An Intraseasonal Mode Linking Wintertime Surface Air Temperature over Arctic and Eurasian Continent

JUNYI XIU,[a,b,c] XIANAN JIANG,[c,d] RENHE ZHANG,[a] WEINA GUAN,[c,e] AND GANG CHEN[f]

[a] *Department of Atmospheric and Oceanic Sciences, Fudan University, Shanghai, China*
[b] *Institute of Atmospheric Sciences, Fudan University, Shanghai, China*
[c] *Joint Institute for Regional Earth System Science and Engineering, University of California, Los Angeles, Los Angeles, California*
[d] *Jet Propulsion Laboratory, California Institute of Technology, Pasadena, California*
[e] *CMA–NJU Joint Laboratory for Climate Prediction Studies, Institute for Climate and Global Change Research, School of Atmospheric Sciences, Nanjing University, Nanjing, China*
[f] *Department of Atmospheric and Oceanic Sciences, University of California, Los Angeles, Los Angeles, California*

(Manuscript received 26 June 2021, in final form 28 November 2021)

ABSTRACT: Key processes associated with the leading intraseasonal variability mode of wintertime surface air temperature (SAT) over Eurasia and the Arctic region are investigated in this study. Characterized by a dipole distribution in SAT anomalies centered over north Eurasia and the Arctic, respectively, and coherent temperature anomalies vertically extending from the surface to 300 hPa, this leading intraseasonal SAT mode and associated circulation have pronounced influences on global surface temperature anomalies including the East Asian winter monsoon region. By taking advantage of realistic simulations of the intraseasonal SAT mode in a global climate model, it is illustrated that temperature anomalies in the troposphere associated with the leading SAT mode are mainly due to dynamic processes, especially via the horizontal advection of winter mean temperature by intraseasonal circulation. While the cloud–radiative feedback is not critical in sustaining the temperature variability in the troposphere, it is found to play a crucial role in coupling temperature anomalies at the surface and in the free atmosphere through anomalous surface downward longwave radiation. The variability in clouds associated with the intraseasonal SAT mode is closely linked to moisture anomalies generated by similar advective processes as for temperature anomalies. Model experiments suggest that this leading intraseasonal SAT mode can be sustained by internal atmospheric processes in the troposphere over the mid- to high latitudes by excluding forcings from Arctic sea ice variability, tropical convective variability, and the stratospheric processes.

KEYWORDS: Arctic; Cold air surges; Cloud radiative effects; Subseasonal variability; Surface temperature

1. Introduction

Subseasonal prediction of extreme weather on the time scale from two weeks to one season has become an active research topic and urgent need in the community due to its immense social benefits for disaster mitigation and risk management (National Academies of Sciences, Engineering and Medicine 2016; Vitart et al. 2017; Vitart and Robertson 2018; Lang et al. 2020). Over the mid- to high latitudes, in particular, extreme events associated with variability in surface air temperature (SAT) greatly affect daily life, public health, energy, industry, and so on. Improved understanding of intraseasonal SAT variability, therefore, can help to advance our capability for subseasonal predictions (e.g., Xiang et al. 2019, 2020).

Recent studies have reported that wintertime SAT exhibits pronounced intraseasonal variability over the mid- to high latitudes of the Northern Hemisphere (NH) (Lin and Brunet 2009; Lin 2015; Yang and Li 2016; Yao et al. 2016; Lin 2018; Guan et al. 2020b; Cui et al. 2020). Two leading intraseasonal modes of winter SAT over the extratropical NH were illustrated by Lin (2018), with one prevailing over North America (NA) and another over Eurasia continent. The leading mode over NA is characterized by a dipole pattern in SAT anomalies with opposite SAT anomaly centers over central NA and East Siberia (ES)/Alaska, respectively (Lin 2015, 2018; Guan et al. 2020b,a). The vertical structure, evolution features, and physical mechanisms of the leading intraseasonal SAT mode over NA have also been documented in detail (Lin 2015; Guan et al. 2020b).

It has been suggested that the leading intraseasonal SAT mode and associated cold surge events over Eurasia and NA could be linked to each other (Lin 2018; Deng et al. 2020; Sung et al. 2021), in which Arctic processes can play a crucial role (e.g., Deng et al. 2020) or possibly through mediation by the North Pacific Oscillation (Sung et al. 2021). While the leading boreal winter intraseasonal SAT variability mode over Eurasia and associated evolution features has been previously examined (e.g., Yang and Li 2016), those studies did not integrally consider the mid- and high latitudes and the Arctic as a whole. Meanwhile, physical processes in sustaining the intraseasonal SAT variability over Eurasia are not completely understood. For example, in addition to temperature advection for the intraseasonal SAT variability as previously suggested (e.g., Yang and Li 2016; Kim et al. 2021), it remains unknown whether the associated cloud–radiative feedback plays a role for the intraseasonal SAT variability, and how temperature anomalies at the surface and in the lower troposphere are coupled with each other, partially due

Corresponding author: Xianan Jiang, xianan@ucla.edu

DOI: 10.1175/JCLI-D-21-0495.1

to the lack of reliable observational dataset for studies on these processes.

The Madden–Julian oscillation (MJO; Madden and Julian 1971, 1972), a dominant intraseasonal variability in the tropics, has been widely reported to exert significant impacts on extratropical intraseasonal SAT variability and extreme weather over the NH continents during boreal winter, including both NA and Eurasia (e.g., Vecchi and Bond 2004; Seo et al. 2016; Cui et al. 2020; Jeong et al. 2005; He et al. 2011; Abdillah et al. 2018; Song and Wu 2019c,b; Li et al. 2020; Song and Wu 2020; Lin and Brunet 2009; Zhou et al. 2012; Riddle et al. 2013; Baxter et al. 2014; Zheng et al. 2018; and many others), and even the Arctic region (Lee et al. 2011; Yoo et al. 2012). For example, cold SAT anomalies and extreme cold surges over East Asia are significantly intensified during the MJO phases 2–3 as defined by the real-time multivariate MJO (RMM) index following Wheeler and Hendon (2004) (e.g., Jeong et al. 2005; Seo et al. 2016). Significant negative SAT anomalies over north Eurasia and the Barents–Kara Sea (BKS) region along with warm SAT anomalies over NA are observed after 1–2 weeks of the enhanced MJO convection over the Indian Ocean (Cui et al. 2020), resembling a so-called NA and the Bering Sea (NABS) leading SAT pattern identified by the self-organizing map analysis in Deng et al. (2020). Abdillah et al. (2018) illustrated that two types of East Asian cold air breaks, a western type and an eastern type, are related to MJO convection over the Maritime Continent (MC) and western Pacific, respectively, as also supported by Song and Wu (2019b). The tropical convective activity associated with the MJO is also found to play a role for the interannual variability of East Asian winter monsoon (e.g., Zhang et al. 2015). However, recent studies on subseasonal predictive skill of mid- to high-latitude SAT anomalies obtained inconsistent results on the role of the MJO. While it was found that MJO status in the model initial condition does not significantly affect subseasonal prediction skill of the NH mid- to high-latitude winter SAT anomalies (Xiang et al. 2019, 2020), slight improvement of predictive skill of SAT anomalies is achieved when strong MJO signals are present in the initial condition for the Eurasia Continent but not NA (Lin 2018).

Influences of the MJO on subseasonal SAT variability over the mid- to high latitudes of Eurasia can also combine with other climate variability modes such as the Arctic Oscillation (AO) or North Atlantic Oscillation (NAO), although these NH annular modes could also be partially linked to tropical convective variability of the MJO (e.g., L'Heureux and Higgins 2008; Lin et al. 2009; Cassou 2008; Jiang et al. 2017). A positive phase of AO/NAO generally corresponds to weakening of the Ural Blocking (Luo et al. 2016), and thus warm SAT anomalies over the East Asia, and vice versa (e.g., Gong et al. 2001; Park et al. 2010, 2011; Geng et al. 2017; Song and Wu 2018, 2019c). It was also reported that the blocking ridges over central and western Siberia that are closely associated with local cold air outbreaks tend to be amplified through interactions between the upper-level Rossby waves and surface cold anomalies (Takaya and Nakamura 2005), indicating that the observed intraseasonal SAT variability over Eurasia can result from internal atmospheric processes over the mid- to high latitudes. Moreover, a recent study by Kim et al. (2021) indicates that variability associated with the Ural blocking can play a critical role, but is not essential for the intraseasonal SAT variability over Eurasia/Arctic.

Stratospheric processes could also play a role in regulating intraseasonal SAT variability over the mid- to high latitudes as suggested by many previous studies, for example, through variability of the stratospheric polar vortex. During the period of weak stratospheric polar vortex, anomalously low SAT is often observed in Eurasia (Kolstad et al. 2010; Woo et al. 2015; Kretschmer et al. 2018; Huang and Tian 2019; Peng et al. 2019; Song and Wu 2019a; Kim et al. 2014; Green and Furtado 2019). Guan et al. (2020b) also suggested a possible interaction between the troposphere and stratosphere associated with the leading intraseasonal SAT mode over NA.

Regardless of the aforementioned studies on plausible roles of tropical convective activity and the stratospheric processes in triggering the intraseasonal SAT variability over the NH mid- to high latitudes, it remains elusive whether these external forcings are essential in generating the observed SAT variability on the intraseasonal time scales. In this study, the leading intraseasonal SAT mode over Eurasia is further examined with a specific focus on its linkage to Arctic processes. Particularly, by capitalizing on realistic simulations of the leading intraseasonal SAT mode in a global climate model, physical processes responsible for the intraseasonal SAT variability over Eurasia are examined. Roles of tropical convective forcing, the stratosphere, and Arctic sea ice variability in sustaining the intraseasonal SAT variability are further explored by model sensitivity experiments. The remainder of this paper is organized as follows. In section 2, the data and methods used in this study are introduced. Structure and evolution features of the observed intraseasonal SAT mode over Eurasia and the Arctic are examined in section 3. In section 4, the intraseasonal SAT mode simulated in a climate model is analyzed and key physical processes are explored based on temperature budget analyses and sensitivity experiments by excluding tropical convective forcing and stratospheric coupling. Conclusions and a summary are presented in section 5.

2. Data and methodology

a. Observational dataset

Daily variables for 1979–2017 from the European Centre for Medium-Range Weather Forecasts (ECMWF) interim reanalysis (ERA-I; Dee et al. 2011) are used in this study. These include SAT, surface pressure (P_S), sea ice concentration (SIC), temperature (T), geopotential height (Z), meridional and zonal winds (u, v), and specific humidity (q) on $0.75° \times 0.75°$ horizontal grids and 37 vertical pressure levels extending from 1000 to 1 hPa. Daily SAT data in China from 2474 stations of the Chinese Meteorological Administration (CMA; available online http://data.cma.cn/) are also analyzed. Analyses in the following will be conducted for the extended boreal winter from November to March. To extract the intraseasonal signals, a 10–90-day bandpass filtering (Duchon 1979)

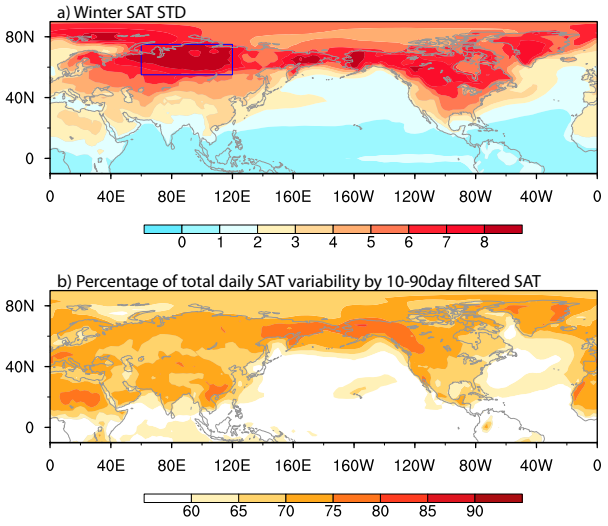

FIG. 1. (a) Standard deviations of daily SAT anomalies (K) during boreal winter (November–March) from 1979 to 2017, and (b) the percentage of total daily SAT STDs explained by 10–90-day filtered SAT anomalies. The blue rectangle in (a) denotes the location over the central North Eurasia continent for spectral analysis shown in Fig. 2.

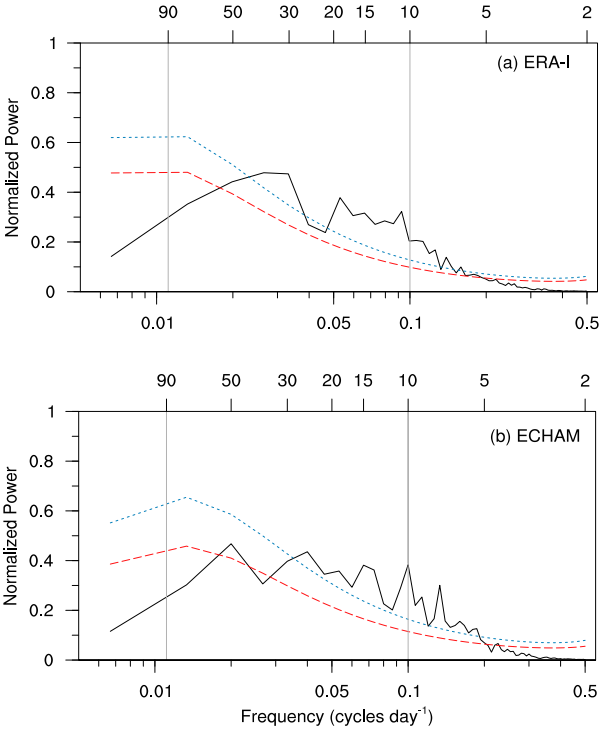

FIG. 2. Power spectra (black) of daily SAT anomalies averaged over the region of 55°–75°N, 60°–120°E (see blue box in Fig. 1a) based on (a) the ERA-I reanalysis and (b) ECHAM AGCM simulations. Red and blue lines denote the Markov red noise spectra and the 95% statistical confidence level, respectively.

is applied to daily anomalies of each variable after removal of the climatological annual cycle (annual mean plus three leading harmonics).

b. Climate model experiments

The atmospheric-only global climate model (GCM) used for this study is the ECHAM AGCM version 4.6 (Roeckner et al. 1996; Jiang et al. 2020), with a resolution of T42 and 19 vertical layers with the model top at 10 hPa. The convection scheme in ECHAM GCM links the cloud-base mass flux to the convective instability for the penetrative convection (Tiedtke 1989; Nordeng 1994). In the control experiment, the model was integrated for 20 years forced by climatological monthly mean sea surface temperature (SST) and sea ice.

Two additional sensitivity experiments are conducted based on ECHAM AGCM to verify the roles of tropical and stratospheric processes in sustaining the intraseasonal SAT variability over Eurasia using a nudging approach. In the first experiment ("no_tropics"), the atmospheric state variables (u, v, T, q) over the tropical region (30°S–30°N) are nudged toward their corresponding climatological annual cycles derived from the control simulations. In the second experiment ("no_strato"), the atmospheric fields above 100 hPa to the north of 40°N are nudged to their climatological annual cycles from the control experiment to exclude influences from the stratosphere. A similar nudging approach has been used to isolate influences of the tropics and midlatitudes on Arctic climate (Ye and Jung 2019), and to explore how Arctic sea ice responds to the observed circulation (Ding et al. 2017).

3. The leading intraseasonal SAT mode over Eurasia and the Arctic region

Figure 1a shows standard deviations (STDs) of daily SAT anomalies during boreal winter over the NH based on ERA-I, in which strong SAT variability over the mid- to high latitudes is clearly evident. A spectral analysis of daily SAT anomalies over the Eurasian region with the maximum daily SAT STD (blue box in Fig. 1a) illustrates pronounced SAT variability on intraseasonal time scales, with two prevailing periods of 10–25 and 25–50 days (Fig. 2a). A significant role of the intraseasonal SAT variability in contributing to the total day-to-day SAT variability based on ERA-I is further confirmed in Fig. 1b, with the ratio of the 10–90-day SAT variability to the total daily STDs exceeding 65% over most of the NH continental regions.

a. Evolution characteristics of the leading intraseasonal SAT mode in observations

To extract the leading intraseasonal SAT mode over Eurasia and the Arctic, an empirical orthogonal function (EOF) analysis is performed based on daily 10–90-day-filtered SAT anomalies from the ERA-I reanalysis over the domain of 20°–90°N, 0°–150°E for the winters from 1979 to 2017. The first EOF mode (EOF_1) accounts for 20% of total SAT variances and is largely characterized by a dipole of SAT anomaly centers with opposite signs, one covering a large portion

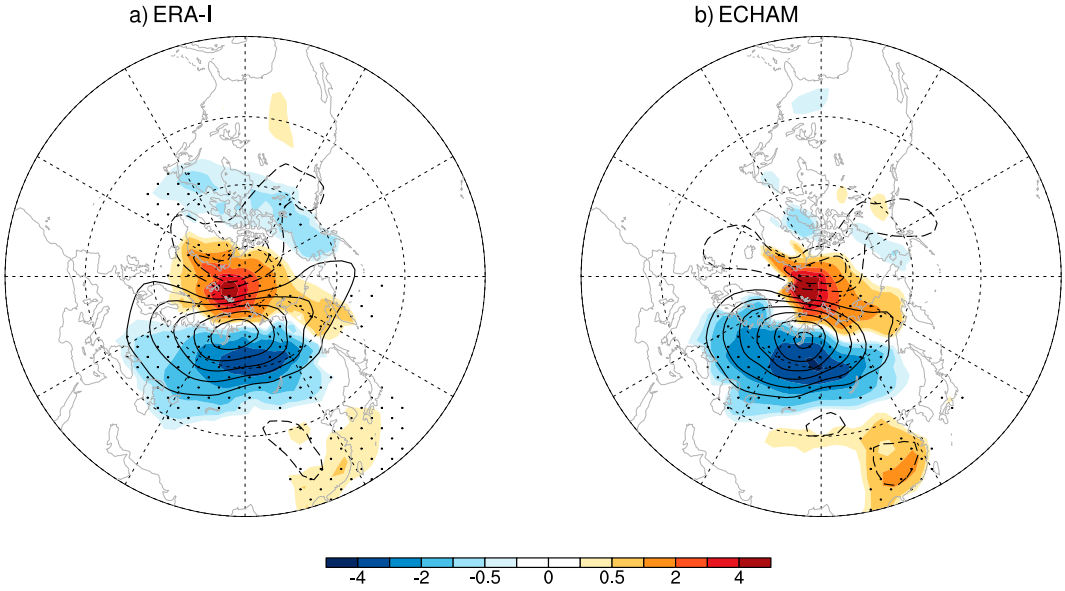

FIG. 3. Regressed anomalous SAT (K; shading) and surface pressure (contours with an interval of 1.0 hPa, dashed if negative with zero contours omitted) against the normalized PC_1 of the leading intraseasonal SAT mode based on (a) the ERA-I reanalysis and (b) ECHAM AGCM simulations. The black dots denote the areas where SAT anomalies are statistically significant at the 95% confidence level.

of north Eurasia and another over the Arctic region (Fig. 3a). Relatively weak SAT anomalies associated with the EOF_1 are also evident over NA, resembling the prevailing North America North Eurasia (NANE) SAT pattern identified in Deng et al. (2020). Cold SAT anomalies over Eurasia and warm SAT anomalies over Arctic associated with the leading intraseasonal SAT mode are linked by an anomalous surface high pressure system based on regressions against the principal component (PC) time series of the EOF_1 (Fig. 3a).

The leading intraseasonal SAT mode as shown in Fig. 3a is largely similar to the leading interannual SAT mode over Eurasia (e.g., Fig. 2a in Mori et al. 2014), suggesting a cross-scale influences of the intraseasonal SAT mode on SAT variability on interannual time scales, similarly as found over the NA sector (Guan et al. 2020a). Mori et al. (2014) also suggests that the anomalous SAT pattern is closely associated with the NAO on the interannual time scale, although there are recent debates on the origin of this interannual SAT mode, particularly regarding the relative role of Arctic sea ice and internal atmospheric processes (e.g., Mori et al. 2019; Blackport et al. 2019; Blackport and Screen 2020).

Figure 4 presents evolution of lag-regressed SAT anomalies associated with the leading intraseasonal SAT mode from day −12 to day 12 with a 3-day interval. Anomalous SAT signals start to amplify after day −9. In corresponding to the establishment of cold anomalies over north Eurasia and warm anomalies over the Arctic at day −6 (Fig. 4c), development of an anomalous surface high centered near the BKS region is observed, suggesting intensification of the Ural blocking high (e.g., Gong et al. 2001; Luo et al. 2016; Takaya and Nakamura 2005). In the following days, both SAT and SLP anomalies associated with the leading SAT mode gradually enhance and peak at day 0 (Figs. 4c–e). After that the leading SAT mode starts to weaken and shifts southeastward (Figs. 4f–h); it starts to dissipate after day 9, suggesting an approximate 3-week period of the leading intraseasonal SAT mode.

b. Vertical structure of the leading intraseasonal SAT mode

In this section, vertical structures of air temperature (T), geopotential height (Z), and wave activity fluxes (WAFs) associated with the leading intraseasonal SAT mode are examined based on lag regressions against the PC_1 of the leading intraseasonal SAT mode. The calculation of 3D WAF is based on the W-vector following Takaya and Nakamura (2001), which is expressed as follows:

$$\mathbf{W} = \frac{p}{2|\mathbf{U}|}\begin{Bmatrix} U\left(\psi'^2_x - \psi'\psi'_{xx}\right) + V\left(\psi'_x\psi'_y - \psi'\psi'_{xy}\right) \\ U\left(\psi'_x\psi'_y - \psi'\psi'_{xy}\right) + V\left(\psi'^2_y - \psi'\psi'_{yy}\right) \\ \frac{f_0^2}{N^2}\left[U\left(\psi'_x\psi'_z - \psi'\psi'_{xz}\right) + V\left(\psi'_y\psi'_z - \psi'\psi'_{yz}\right)\right] \end{Bmatrix},$$

where ψ' is the perturbation streamfunction, derived based on lag regressions of 10–90-day filtered winds against the PC_1 of the leading SAT mode; U and V are winter mean zonal and meridional winds, respectively; f_0 is the Coriolis parameter; N^2 is the buoyancy frequency; p is the normalized pressure by 1000 hPa; and the subscripts represent partial derivatives in the corresponding x, y, and z directions.

Figure 5 illustrates the height–latitude cross sections of lag-regressed anomalies of T, Z, and WAF averaged over 85°–95°E and 85°–95°W for the Eurasian and NA sectors from day −12 to day 9. At day −9, before significant T anomalies associated

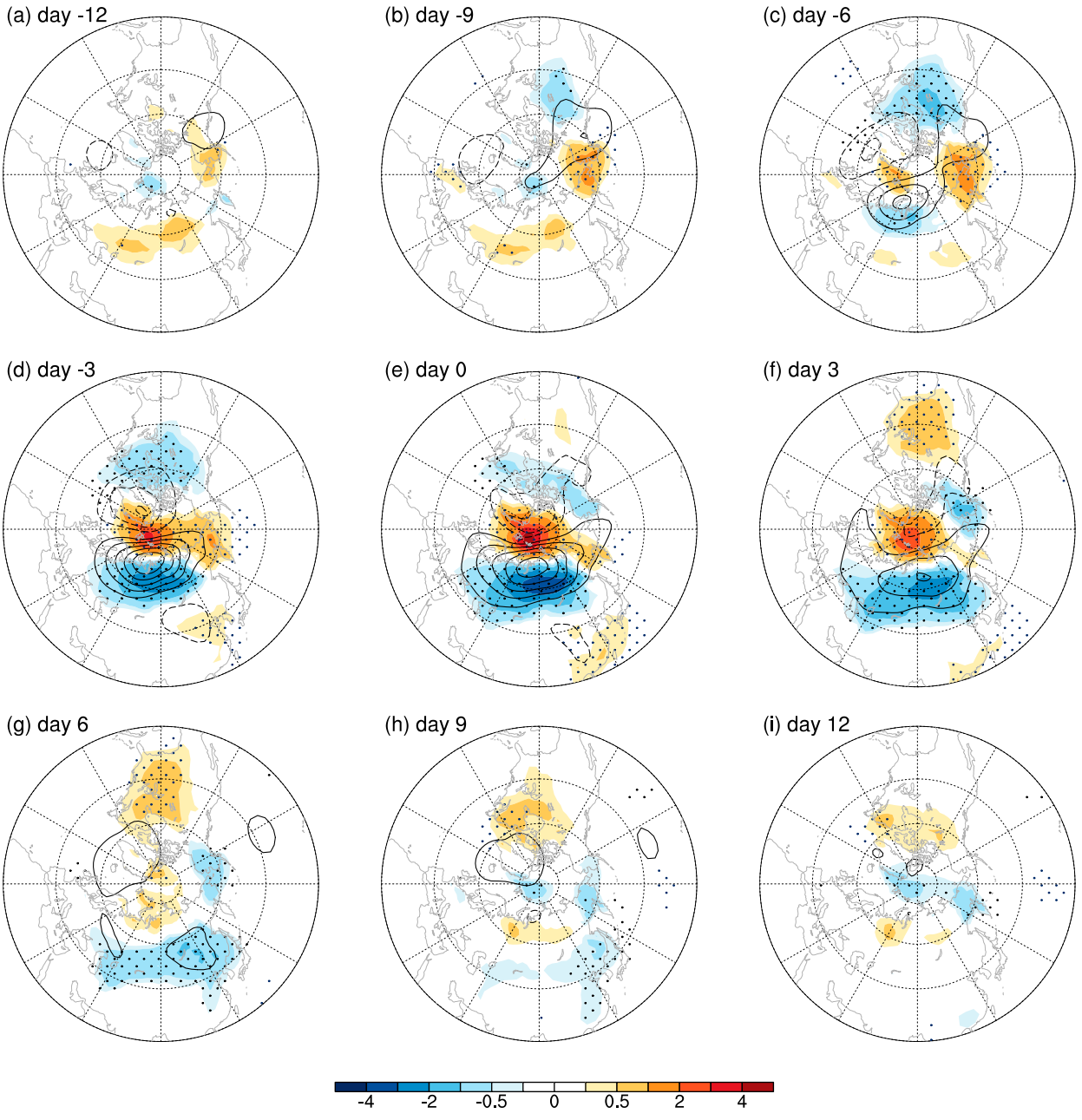

FIG. 4. Lead–lag regressions of anomalous SAT (K; shading) and surface pressure (contours with intervals of 1.0 hPa with zero contours omitted) onto the normalized PC_1 of the leading intraseasonal SAT mode based on the ERA-I reanalysis. Areas with black dots indicate the SAT anomalies surpassing the 95% statistical significance level. The black dots denote the areas where SAT anomalies are statistically significant at the 95% confidence level.

with the leading SAT mode appear over the Eurasian sector, cold anomalies have developed over NA near 60°N in the troposphere and is coupled with negative Z anomalies vertically extending to 50 hPa (Fig. 5b). Meanwhile, positive Z anomalies is found over the upper stratosphere near the Arctic region in both Eurasia and NA sectors. After day −9, positive stratospheric Z anomalies near the Arctic extend downward into the lower troposphere between 75° and 90°N over Eurasia accompanying with the establishment of warm temperature anomalies between the surface and 300 hPa near the Arctic (Fig. 5c), suggesting a possible role of the stratosphere in amplifying the intraseasonal T anomalies in the lower troposphere and at the surface. At the same time, initiation of negative Z anomalies is evident over Eurasia near 60°N at 300 hPa associated with local development of cold anomalies in the lower troposphere (Fig. 5c), which is consistent with convergence of the

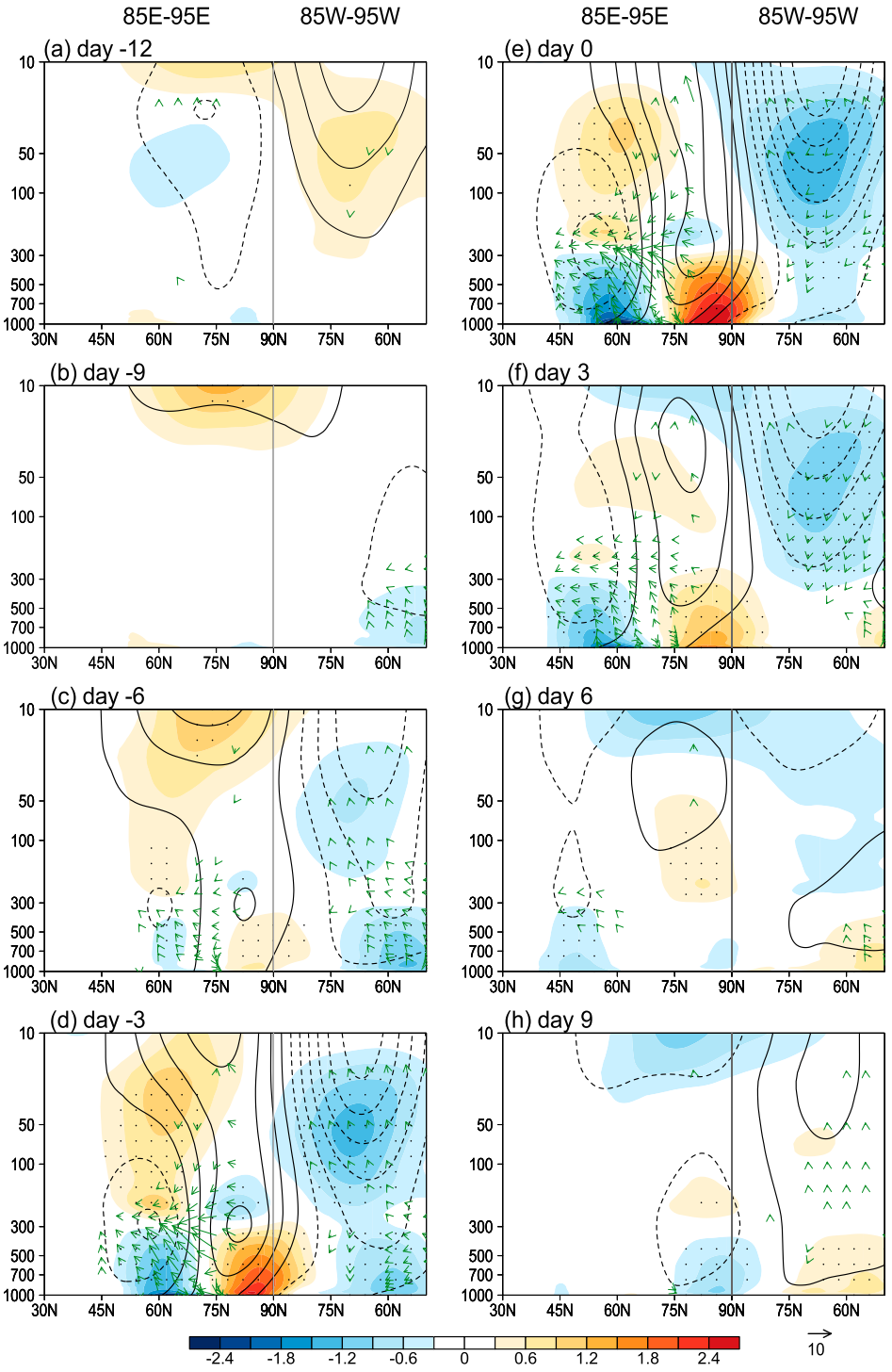

FIG. 5. Height–latitude cross sections of lag-regressed anomalies of T (K; shadings, see color bar below), Z (gpm; contours with an interval of 20 gpm), and WAF (vectors; $m^2\ s^{-2}$ for the horizontal component and $1.0 \times 10^{-3}\ m^2\ s^{-2}$ for the vertical component; only plotted on grids where the amplitude of zonal component is greater than $1\ m^2\ s^{-2}$) averaged over 85°–95°E and 85°–95°W for the Eastern and Western Hemispheres, respectively. The black dots denote the areas where Z anomalies are statistically significant at the 95% confidence level.

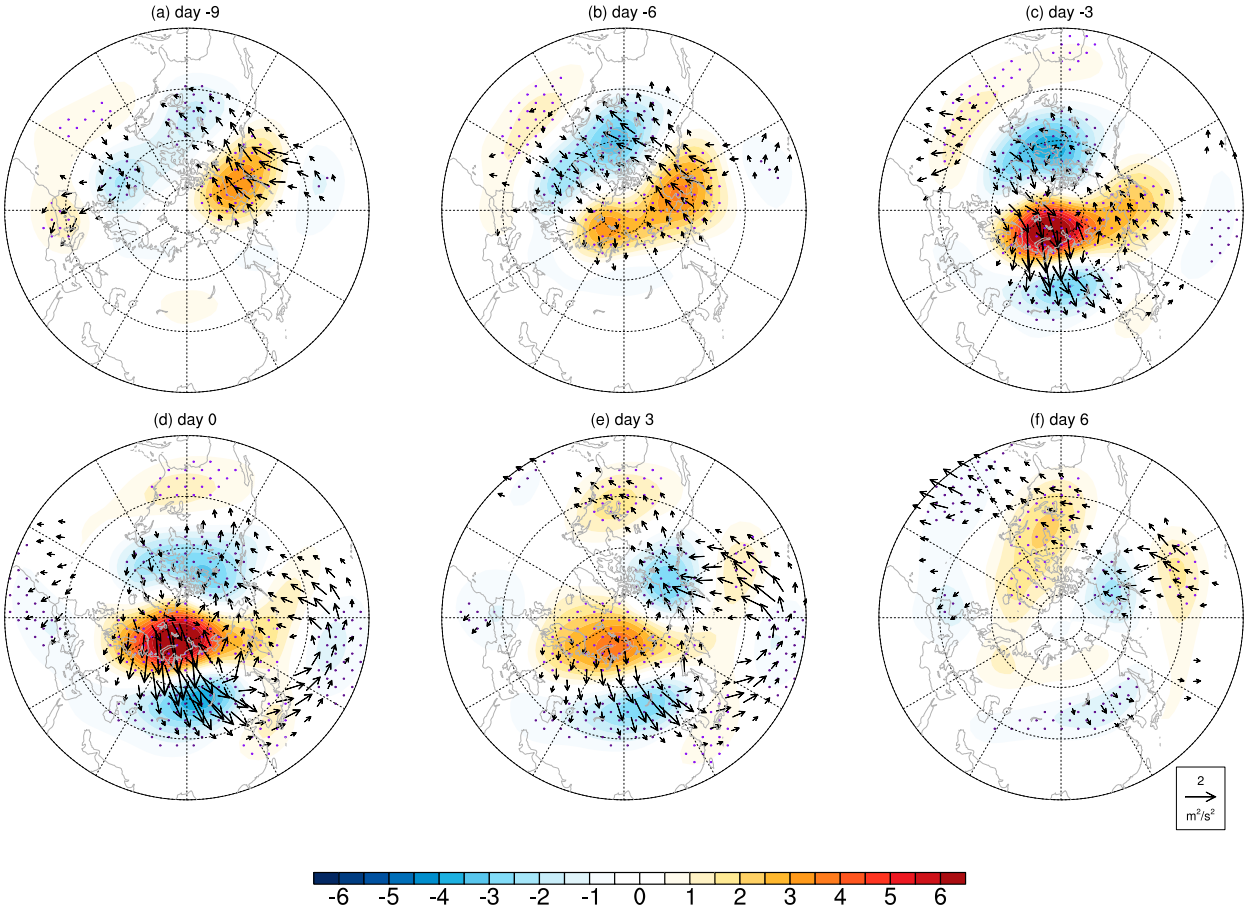

FIG. 6. Regressed anomalies of geopotential height (gpm; shading) and horizontal wave activity fluxes ($m^2\ s^{-2}$; vectors; only plotted on grids where the amplitude is greater than 0.2 $m^2\ s^{-2}$) at 250 hPa onto the normalized PC_1 of the leading intraseasonal SAT mode based on the ERA-I reanalysis. The black dots denote the areas where Z anomalies are statistically significant at the 95% confidence level.

southward WAF fluxes from the Arctic region as more clearly seen at day −3 (Fig. 5d). On the other hand, the negative Z anomalies also dramatically intensify over the NA sector and vertically stretch from the surface all the way to the upper stratosphere after day −6. In the following days, both circulation and T anomalies, and associated WAF fluxes significantly intensify and peak at day 0. Warm and cold anomalies are observed over the Arctic region and Eurasian continent near 60°N, respectively, from the surface to 300 hPa, with the maximum amplitude in T anomalies occurring near the surface. In contrast, T anomalies show opposite sign in the upper troposphere above 300 hPa and the stratosphere (Figs. 5c–f). After day 0, warm T anomalies start to emerge over the NA sector near 60°N while circulation and T anomalies over the Arctic region and Eurasia weaken and change sign after day 6 (Figs. 5g,h).

The establishment of positive geopotential height anomalies in the troposphere over the Eurasian sector between 75° and 90°N after day −6 as discussed in Fig. 5 is further illustrated by time evolution of Z anomalies and WAF at 250 hPa (Fig. 6). It is illustrated that initiation of positive Z anomalies at 250 hPa near the Arctic region over the Eurasian sector at day −6 is linked to northward WAFs over the Atlantic Ocean with positive and negative Z anomalies over the subtropical and North Atlantic Ocean, respectively, resembling the wave pattern associated with the positive phase of the NAO. After day −6, the NAO-like wave pattern disappears over the Atlantic associated with rapid amplification of positive Z anomalies near the Arctic; meanwhile, strong WAFs that direct southward from the Arctic to north Eurasia are induced, which tend to trigger the initiation of negative Z anomalies over Eurasia continent (Figs. 6c–e, also Figs. 5c–f). A statistically significant although weak positive correlation between the NAO index and PC_1 of the intraseasonal SAT mode is confirmed near day −6 (figure not shown).

c. Influences of the leading intraseasonal SAT mode

The leading intraseasonal SAT variability mode over Eurasia and associated circulation anomalies exhibit widespread influences on weather and climate as previously reported (e.g., Yang and Li 2016; Yang et al. 2019; Cui et al. 2020). For an example to illustrate how this intraseasonal SAT mode can be potentially useful for subseasonal-to-seasonal prediction over regions away from north Eurasia and the Arctic, Fig. 7

shows lag regressions of 10–90-day-filtered SAT anomalies in China based on station observations. Significant modulation of the leading intraseasonal SAT mode on subseasonal temperature variations over China is clearly evident, possibly associated with its southeastward migration discussed in Fig. 2, as also reported in previous studies (e.g., Yao et al. 2015; Yao et al. 2020). From day −12 to day −6, positive SAT anomalies largely prevail over north China associated with the leading SAT mode. At day −3, negative SAT anomalies begin to appear over the northeast and northwest China and then greatly amplify and extend southward to about 40°N. The maximum amplitude of SAT anomalies is observed between day 3 and day 6 with an amplitude greater than 0.5°C. Note that the minimum SAT anomalies over the mid- to high latitudes associated with the leading intraseasonal SAT mode leads the minimum SAT anomalies in China by about 6 days, indicating a potential role of the leading SAT mode for subseasonal SAT predictions in China.

In addition to its direct impact on SAT, the leading intraseasonal SAT mode and associated circulation pattern can also significantly influence Arctic sea ice. Motivated by the study on the relationship between circulation and Barents Sea ice conditions on the subseasonal time scale in Sorokina et al. (2016), we also analyzed the linkage of SIC variability over the BKS region to the leading intraseasonal SAT mode. Figure 8 illustrates lag regressions of 10–90-day-filtered SIC anomalies onto the PC_1 of the intraseasonal SAT mode. Associated with the warm SAT anomalies over the Arctic and cold anomalies over north Eurasia from day −3 to day 9, reduced SIC anomalies over the BKS region are observed. Note that the peak of negative SIC anomalies is observed at day 3 (Fig. 8d) but the maximum positive (negative) SAT anomalies over the Arctic (Eurasia) and associated pressure anomalies at day 0 (Fig. 4e), indicating that circulation anomalies associated with the leading SAT mode slightly lead SIC variability as also reported in Sorokina et al. (2016). On the other hand, reduced SIC over the BKS may also enhance the warm SAT anomalies over the Arctic and cold anomalies over Eurasia associated with the leading SAT mode by inducing an anticyclonic circulation over Siberia through tropospheric Rossby wave responses (e.g., Honda et al. 2009; Inoue et al. 2012; Mori et al. 2014; Nakamura et al. 2015), or through a stratospheric pathway via vertically propagating planetary waves (Kim et al. 2014; Sun et al. 2015; Nakamura et al. 2016; Zhang et al. 2018).

As previously discussed, many previous studies hypothesized that tropical convective activity associated with the MJO could play a role in triggering the intraseasonal SAT variability over the mid- to high latitudes of Eurasia (e.g., Jeong et al. 2005; Seo et al. 2016; Cui et al. 2020). Therefore, lag-regressed precipitation patterns associated with the intraseasonal SAT mode are similarly examined, but the result does not support a close association between the eastward propagating MJO signals along the equator and the leading intraseasonal SAT mode over Eurasian and the Arctic (figure not shown). This result, therefore, suggests that the leading intraseasonal SAT mode over Eurasia and the Arctic may not be directly related to the MJO.

4. Key processes of the leading intraseasonal SAT mode based on ECHAM simulations

While the observed characteristics and vertical structure of the leading intraseasonal SAT mode are illustrated in the previous section, key processes in sustaining this intraseasonal SAT variability mode are not fully understood. Critical questions include whether the cloud–radiative feedback plays an important role in sustaining the vertical T structure associated with the leading SAT mode. How are T anomalies in the troposphere coupled with temperature variability near the surface during the evolution of the intraseasonal SAT mode as shown in Fig. 5? Are forcing signals from the stratosphere and tropical convective activity essential in generating the leading intraseasonal SAT variability mode over north Eurasia and the Arctic? These questions are to be addressed in this section based on ECHAM AGCM simulations.

a. The leading intraseasonal SAT mode in ECHAM simulations

Figure 2b illustrates the prevailing periodicity of SAT variability over Eurasian Continent in ECHAM AGCM simulations, which captures the observed high-frequency intraseasonal variability (≤30 days), but largely misses the 25–50-day low-frequency intraseasonal variability in the observations (Fig. 2a). The spatial pattern of the leading intraseasonal SAT mode and associated circulation anomalies in ECHAM AGCM simulations are further shown in Fig. 3b following a similar EOF analysis, which greatly resemble the observed counterpart, including cold anomalies over north Eurasia and warm anomalies over the Arctic region as well as the anomalous high in-between the two SAT anomaly centers. The observed SAT anomalies over the NA sector associated with the leading intraseasonal SAT mode (Fig. 3a), however, are not simulated in GCM, suggesting the signals over NA may not be essential in generating the intraseasonal SAT mode over Eurasia. Figure 9 further illustrates evolution of the leading SAT mode in model simulations, which again shares great similarity to the observations shown in Fig. 4. For example, initiation of the negative SAT anomalies over north Eurasia is associated with the development of an anomalous high near the BKS region from day −9 to day −6 (Figs. 9b,c). After that, both SAT and circulation anomalies dramatically intensify and reach the strongest amplitudes at day 0 and then gradually decay in the following days.

Similarly as in Fig. 5 for the observations, the meridional–vertical cross sections of the regressed T, Z, and WAF anomalies averaged over 85°–95°E and 85°–95°W associated with the leading SAT mode based on ECHAM simulations are illustrated in Fig. 10. The evolution of T anomalies in the troposphere is largely consistent with the observations. From day −6 to day 3, positive (negative) T anomalies are evident over the Arctic (north Eurasia) region extending from the surface to 300 hPa (shading in Figs. 10c–f) with the peak amplitude at day 0. The T anomalies in the upper troposphere and stratosphere with a largely opposite sign to those in the lower troposphere are also simulated in ECHAM, similar to the observations. Some differences in the vertical structure of circulation anomalies between model simulations and

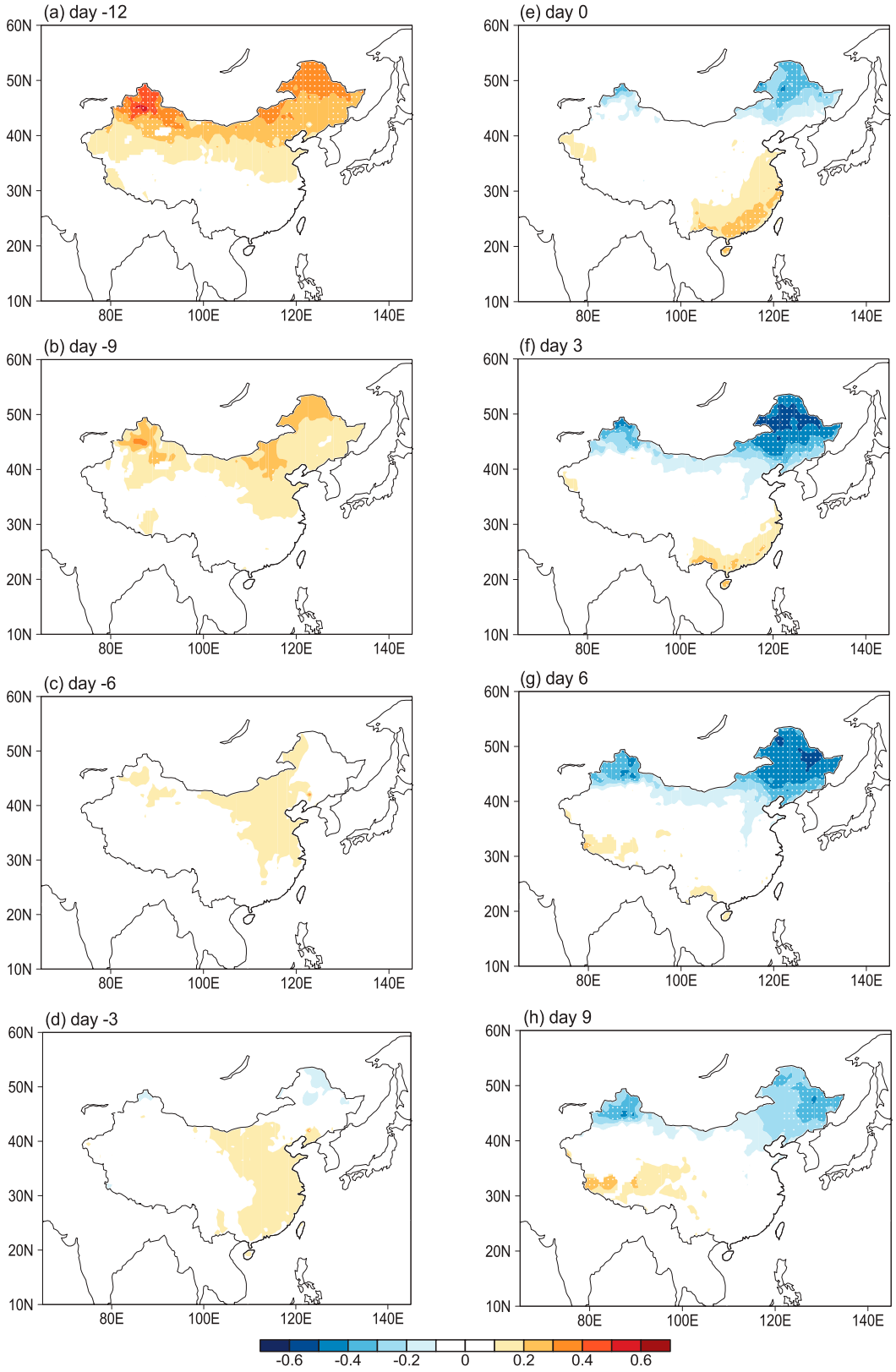

FIG. 7. Lead–lag regressions of 10–90-day filtered SAT (K) in China onto the normalized PC_1 of the leading intraseasonal SAT mode from day −12 to day 9. The dots denote the areas that are statistically significant at the 95% confidence level.

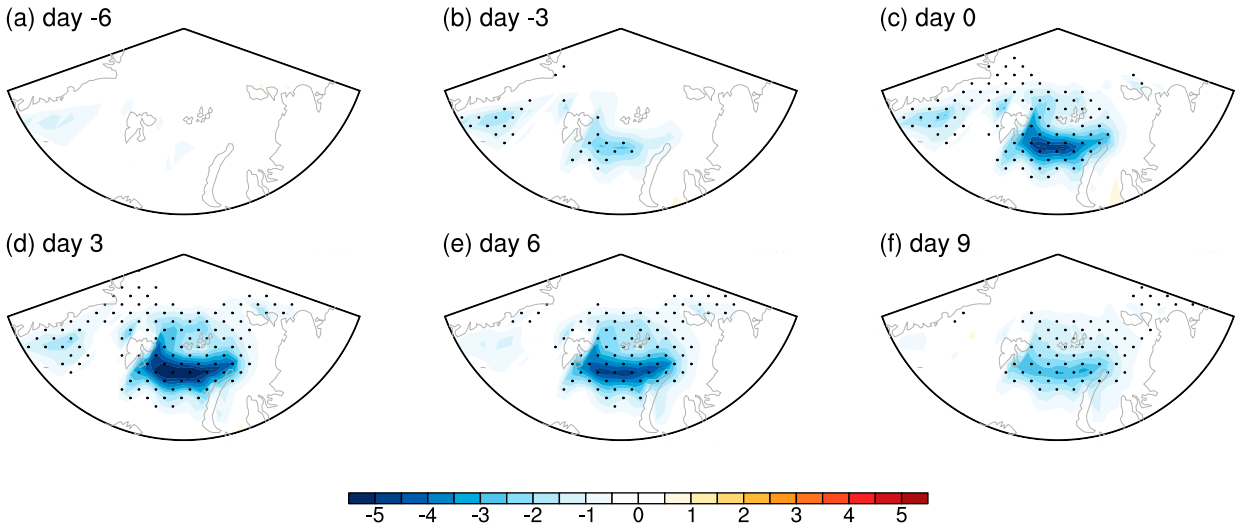

FIG. 8. As in Fig. 6, but for lead–lag regressions of 10–90-day filtered sea ice concentration anomalies (%) over the Eurasian sector of the Arctic region from day −6 to day 9. The black dots denote the areas that are statistically significant at the 95% confidence level.

observations, however, are also readily seen. For example, the observed T and circulation anomalies over the NA sector associated with the intraseasonal SAT mode are greatly underestimated in GCM simulations. Also as previously mentioned, associated with development of warm SAT anomalies over the Arctic after day −9, a downward extension of circulation anomalies from the stratosphere to lower troposphere is observed (Fig. 5c), but this process is not evident in simulations. Instead, the maximum Z anomalies are found near 300 hPa throughout the evolution of the leading intraseasonal SAT mode in simulations. This difference could be due to the low-top configuration in the ECHAM model used in this study, such that interactions between the stratosphere and troposphere are not able to be well depicted. Nevertheless, the largely well simulated leading intraseasonal SAT mode and its associated circulation anomalies in this model itself may suggest that coupling with the stratosphere is not essential for this intraseasonal SAT mode. This will be further discussed with model sensitivity experiments.

Evolution of anomalous Z and WAF at 250 hPa associated with the leading intraseasonal SAT mode in model simulations is further illustrated in Fig. 11 to facilitate a comparison to the observations (Fig. 6). The most important observed features of the intraseasonal SAT mode, including the establishment of positive Z anomalies over the Arctic region of the Eurasian sector at day −6, and the southward WAFs from the Arctic to north Eurasia associated with the development of negative Z anomalies over Eurasia continent are well simulated in the model. However, the NAO-like wave pattern along with the northward WAFs into the Arctic over the Atlantic Ocean at day −6 in the observations is absent in model simulations (cf. Figs. 6b and 11b), indicating the amplification of Z anomalies near the Arctic at day −6 associated with the intraseasonal SAT mode may not necessarily be related to the Rossby wave sources associated with the NAO-like wave pattern over the Atlantic Ocean.

b. Temperature budget analysis in the troposphere

Since ECHAM GCM well captures the most important characteristics and vertical structure of the observed leading intraseasonal SAT mode, diagnoses based on GCM simulations can provide important insights into the key processes of the intraseasonal SAT mode. As previously discussed, in both observations and simulations the warm T anomalies over the Arctic region and cold T anomalies over Eurasia in the lower troposphere starts after day −9 and reach their maximum amplitude at day 0. In the following, we examine the total T tendency pattern and associated budget terms from day −8 to day 0 based on ECHAM simulations to determine the critical processes responsible for the development of the leading SAT mode.

The total T tendency in the free atmosphere can be depicted by the temperature equation on the p coordinate:

$$\frac{\partial T}{\partial t} = -u\frac{\partial T}{\partial x} - v\frac{\partial T}{\partial y} - \omega\frac{\partial T}{\partial p} + \frac{\kappa T\omega}{p} + Q_{\text{diab}}, \qquad (1)$$

where u, v and T are regular variables; ω is the vertical velocity under the p coordinate; $\kappa = R_d/C_{pd}$ with R_d and C_{pd} the gas constant and specific heat of dry air, respectively; and Q_{diab} denotes the diabatic processes including convective and radiative heating, and vertical diffusion due to turbulences. In the following discussions, the sum of the first four terms on the rhs of Eq. (1), i.e., the zonal, meridional, and vertical T advection, as well as the adiabatic term $\kappa T\omega/p$, is defined as the total dynamic process.

Figure 12a illustrates the height–latitude cross sections of total T tendency anomalies from day −8 to day 0 derived by regressions again the PC_1 of the leading intraseasonal SAT mode based on ECHAM simulations. Consistent with the vertical structure of T anomalies at day 0 (Fig. 10e), warming over the Arctic region and cooling over Eurasia below 300 hPa are clearly seen from day −8 and day 0, along with an opposite sign in T tendency above 300 hPa. Figures 11b–d also presents

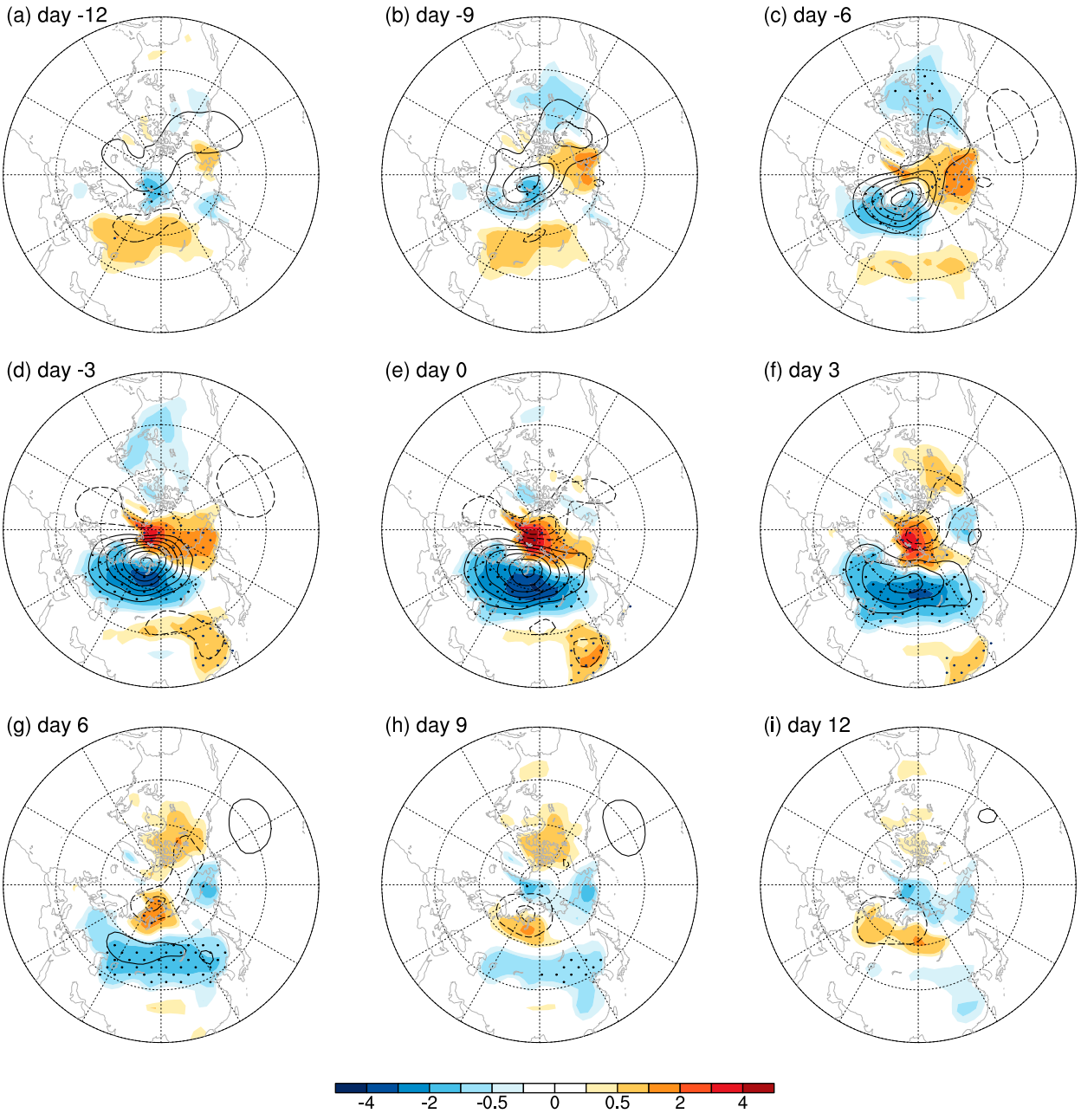

FIG. 9. As in Fig. 4, but based on the control experiment by the ECHAM AGCM.

decomposition of the total T tendency pattern into several major budget terms due to dynamics (horizontal/vertical advection and adiabatic processes), radiation (longwave and shortwave radiation), and convection (subgrid cumulus and gridscale condensation) based on model output. It is readily seen that the atmospheric dynamic processes play a primary role in driving the leading intraseasonal temperature mode, while amplitudes of the other two terms are generally weak. Note that the T tendency anomalies due to vertical diffusion is rather weak and not well organized (figure not shown), therefore, the strong coupling between the vertically extended T anomalies in the free atmosphere and near the surface associated with the leading intraseasonal SAT mode as shown in Figs. 5 and 10 is not directly due to the vertical mixing.

Relative roles of each T budget term can be further quantitatively assessed based on ECHAM simulations by projecting their corresponding patterns onto the vertical–latitude cross-section of the total T tendency over 1000–300 hPa (i.e., the blue box in Fig. 12a). The projection coefficients from each term as shown by the gray bars in Fig. 12 further suggests that the dynamic process plays a crucial role in amplifying the intraseasonal SAT mode. In agreement with previous discussions, convective and

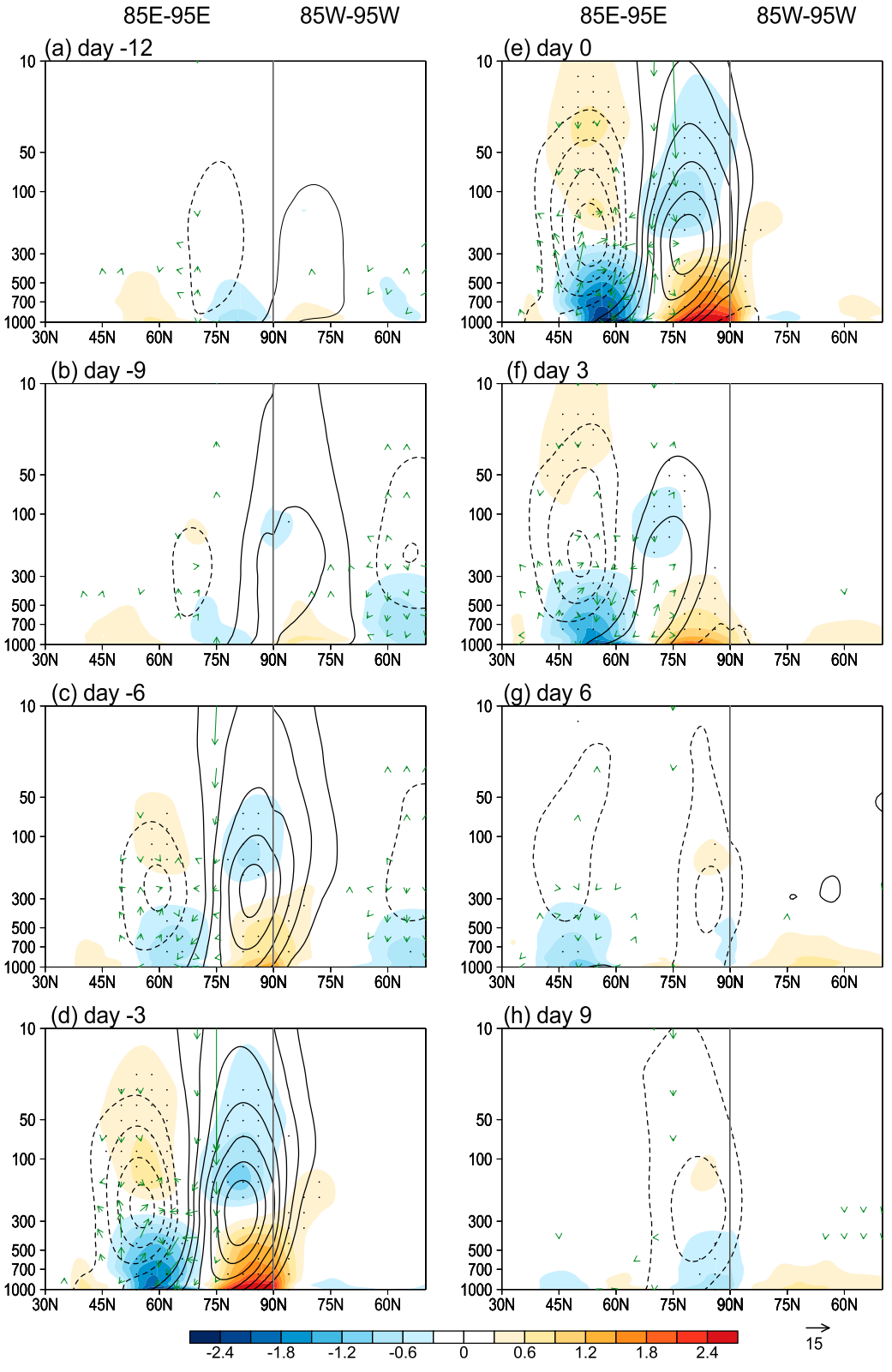

FIG. 10. As in Fig. 5, but based on ECHAM AGCM simulations.

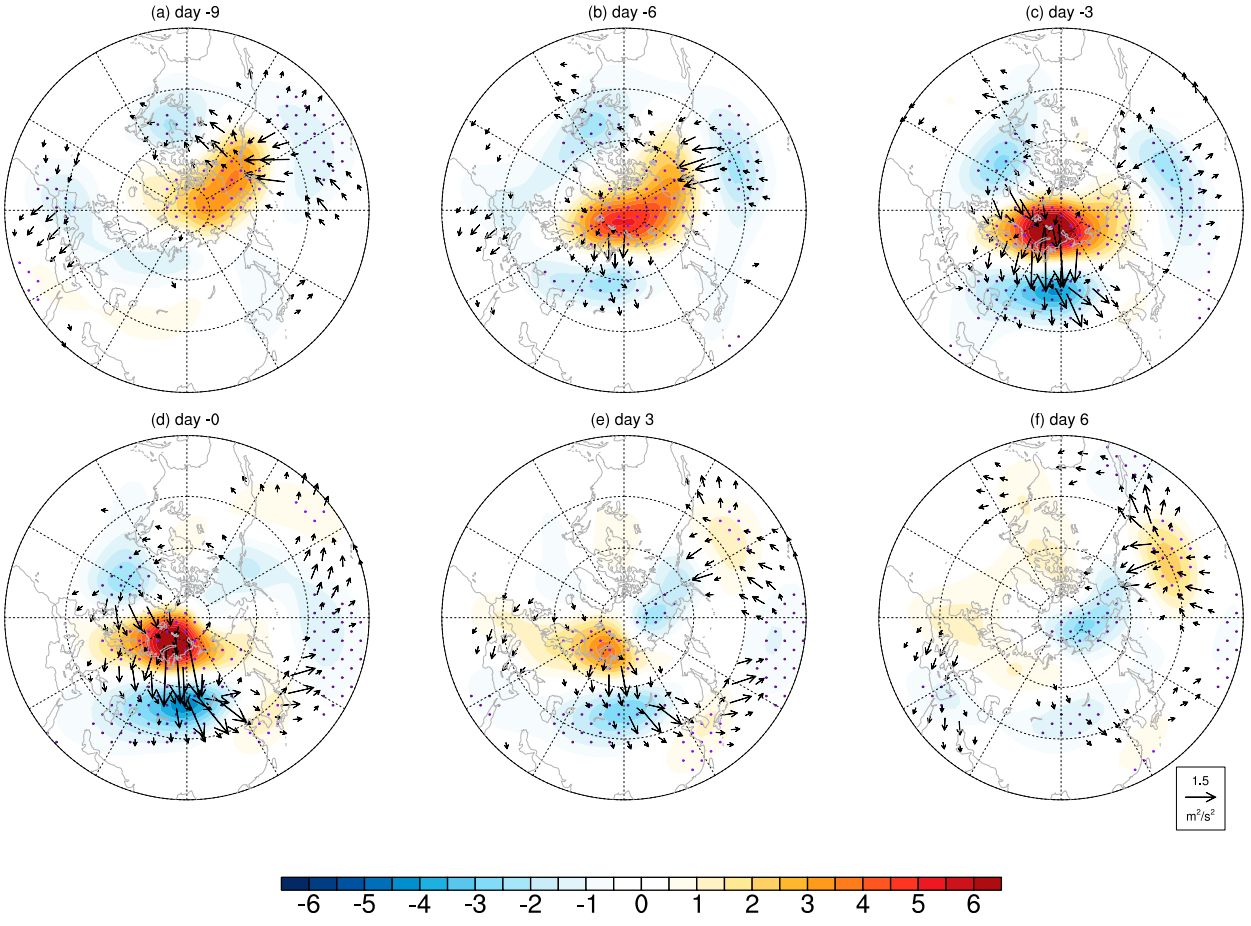

FIG. 11. As in Fig. 6, but based on the control experiment based on the ECHAM AGCM.

radiative effects are not important for development of the intraseasonal SAT mode. The important role of dynamic processes for the total T tendency is also confirmed in the observations by applying a same approach (blue bars in Fig. 13). Note that contributions from the radiative and convective effects cannot be assessed based on ERA-I due to the unavailability of these data.

Further analysis based on both observations and model simulations suggests that the zonal and meridional T advection are both important for the total T tendency anomalies due to the dynamic processes, which are mainly associated with advection of mean temperature pattern by anomalous circulation associated with the intraseasonal SAT mode. To demonstrate this process, Fig. 14 illustrates 1000–300-hPa vertically averaged winter mean T (shaded), intraseasonal T anomalies (contours), and horizontal wind anomalies (vectors) averaged from day −8 to day 0. In both simulations (Fig. 14a) and observations (Fig. 14b), the winter mean temperature in the mid- to high latitudes of NH is characterized by a minimum over the Arctic region with strong meridional gradient. Given an anticyclonic circulation over north Eurasia associated with the intraseasonal SAT mode, northerly wind anomalies tend to bring cold air from Arctic to the Eurasian continent, while southerly wind anomalies act to bring warmer air over the lower latitudes into the Arctic, contributing to the warm anomalies over the Arctic region and cold anomalies over Eurasia.

c. Temperature budget analysis at the surface

As the above model results indicate that the vertical mixing does not play a role in generating the coherent vertical temperature variability associated with the intraseasonal SAT mode, a critical question therefore remains unanswered regarding the key process for the strong coupling of surface temperature and air temperature anomalies in the lower troposphere (Figs. 5 and 10). To address this question, we further conduct a budget analysis for surface temperature based on ECHAM GCM simulations. Following Clark and Feldstein (2019) for a study on surface temperature analysis associated with the NAO, changes on the intraseasonal time scale in skin temperature (T_s) can be expressed under the assumption of the infinitely thin interface at the surface:

$$T_s' = \left(F_{\mathrm{lw}}^{\downarrow\prime} + F_{\mathrm{sw}}^{\downarrow\prime} + F_{\mathrm{sw}}^{\uparrow\prime} + F_{\mathrm{sh}}' + F_{\mathrm{lh}}' + R'\right) \Big/ 4\varepsilon_s \sigma \overline{T_s}^3, \qquad (2)$$

where primes denote anomalies associated with the intraseasonal SAT mode; F_{lw} and F_{sw} indicate longwave and

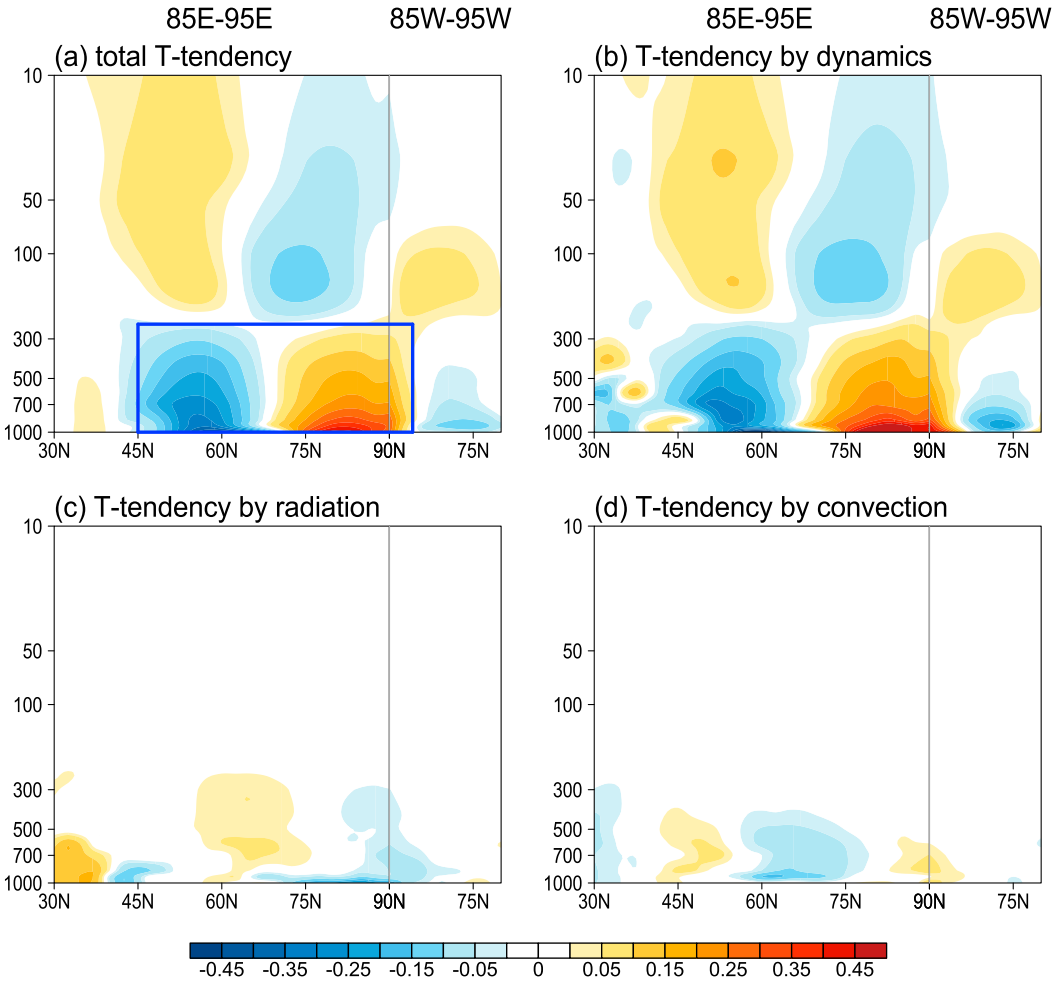

FIG. 12. Height–latitude cross sections of 10–90-day filtered (a) total T-tendency anomalies, and budget components by (b) dynamics (horizontal and vertical advection, and the adiabatic process), (c) radiation (longwave and shortwave), and (d) convection (cumulus plus gridscale precipitation) averaged from day −8 to day −1 based on ECHAM simulations. All these anomalies (K day^{-1}) are derived by lag regressions of their corresponding 10–90-day filtered fields against the normalized PC_1 of the leading intraseasonal SAT mode.

shortwave radiation, respectively; and F_{sh} and F_{lh} for sensible and latent heat fluxes at the surface, respectively. The arrows "↑" and "↓" refer to the upward and downward directions for the energy fluxes, respectively. The term ε_s is the surface emissivity, σ is the Stefan–Boltzmann constant, and $\overline{T_s}$ denotes the winter mean skin temperature; R represents other remaining surface energy budget processes, such as T_s changes associated with conduction due to ice melting, etc., which is not provided by ERA-Interim but available from ECHAM output.

Based on Eq. (2), the relative role of each term on the right-hand side for T_s changes associated with the intraseasonal SAT mode can be examined based on both observations and model simulations. As spatial pattern of T_s is largely identical to the SAT pattern associated with the leading intraseasonal SAT mode (figure not shown), in the following we compare various energy flux patterns against the SAT pattern (Fig. 15). Due to its rather weak amplitude over the mid- to high latitudes of NH during boreal winter, shortwave radiation variability associated with the intraseasonal SAT mode is not shown. Both modeling and observational results in Fig. 15 clearly illustrate that the $F_{lw}^{\downarrow\prime}$ term, i.e., the downward longwave radiation (DLWR) at the surface, plays a dominant role in driving the surface temperature variability associated with the leading intraseasonal SAT mode. The anomalous DLWR patterns associated with the leading SAT mode at day 0 are highly consistent with the anomalous SAT spatial distributions in both ECHAM simulations (Fig. 15a) and ERA-I (Fig. 15b), with enhanced DLWR anomalies collocated with warm anomalies over the Arctic region, and reduced DLWR over the regions of negative SAT anomalies over north Eurasia.

To further investigate the processes responsible for the DLWR anomalies, the total DLWR anomalies at day 0 are decomposed into components associated with clear-sky and

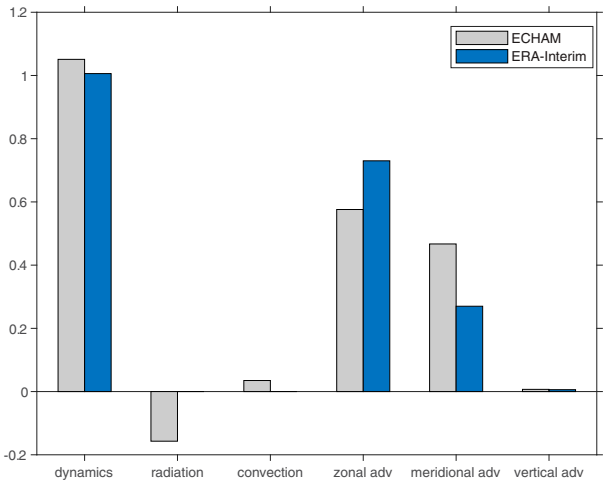

FIG. 13. Contribution of each T tendency term to the total T tendency represented by projection coefficient of its spatial pattern onto the total T tendency pattern over the 2D latitude–height plane (the green box in Fig. 11a). Note that the adiabatic term is combined with the vertical advection in this plot [see Eq. (1)]. Gray bars are for ECHAM GCM simulations, and blue bars for ERA-I. Radiative and convective heating terms are not available from ERA-I.

cloudy conditions based on ECHAM simulations (Fig. 16). The amplitude of clear-sky DLWR anomalies is found be very weak (Fig. 16a), and the total DLWR anomalies are primarily contributed by the cloud-induced DLWR (Fig. 16b). This is further supported by distribution of simulated cloud fraction anomalies in Fig. 16c, which suggests a close association between reduced (enhanced) cloud fractions at 925 hPa and surface cooling (warming) anomalies. The reduced (enhanced) clouds associated with the leading intraseasonal SAT mode are found to be largely consistent with reduced (enhanced) moisture anomalies at 925 hPa (Fig. 16d), suggesting that the increased moisture over the Arctic region indirectly intensifies surface warming through increased clouds and thus enhanced DLWR, and opposite for the cooling anomalies over north Eurasia. Further analysis suggests that the anomalous moisture pattern as shown in Fig. 16d is also due to advection of winter mean moisture pattern by the anomalous winds associated with the intraseasonal SAT mode similarly as for T anomalies (figure not shown).

d. Roles of the tropics and stratosphere for the leading intraseasonal SAT mode

As the leading intraseasonal SAT mode and associated processes are largely well captured in the control experiment based on ECHAM GCM, roles of stratospheric processes and tropical convective activity on the leading intraseasonal SAT mode are further investigated by two additional sensitivity experiments. In the first experiment, "no_tropics," the intraseasonal variability over the tropics is eliminated by relaxing model variables to climatological annual cycle derived from the control experiment; while in the second experiment, "no_strato," influences of the stratospheric variability above 100 hPa to the north of 40°N is eliminated using a similar nudging approach. Figure 17 displays the leading SAT modes using similar EOF analyses based on the "no_tropics" and "no_strato" experiments along with that from the control experiment based on ECHAM AGCM. The results suggest that the leading intraseasonal SAT mode over Eurasia and the Arctic in the two sensitivity experiments (Figs. 17b,c) are

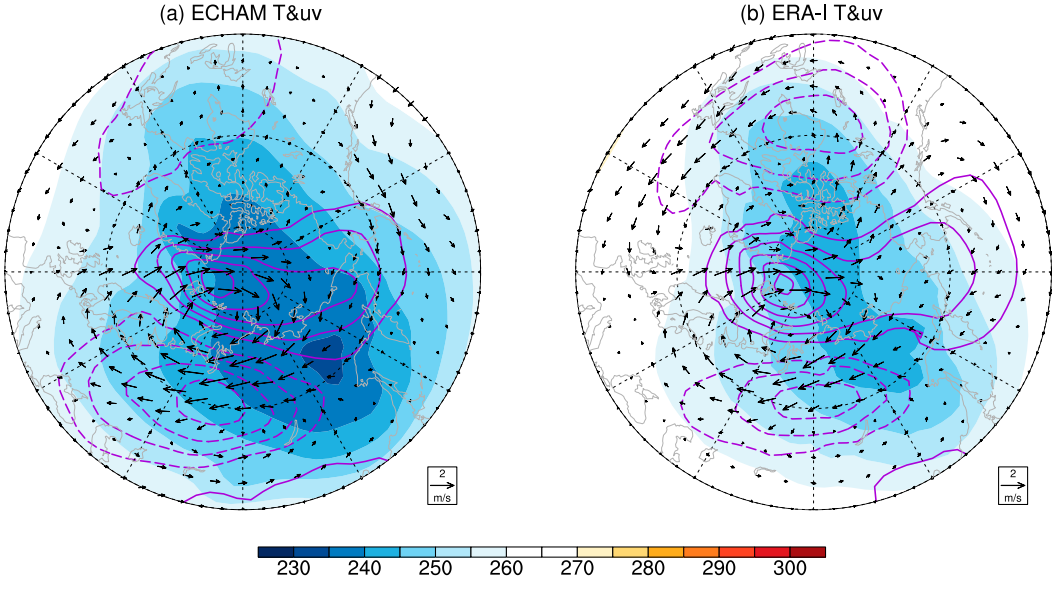

FIG. 14. Distributions of 1000–300-hPa averaged winter mean temperature (shading; K), the intraseasonal T anomalies (contours; K) and intraseasonal horizontal wind anomalies (vectors; m s^{-1}) averaged from day −8 to day 0 derived by regressions against the normalized PC_1 of the leading intraseasonal SAT mode in (a) ECHAM simulations and (b) ERA-I.

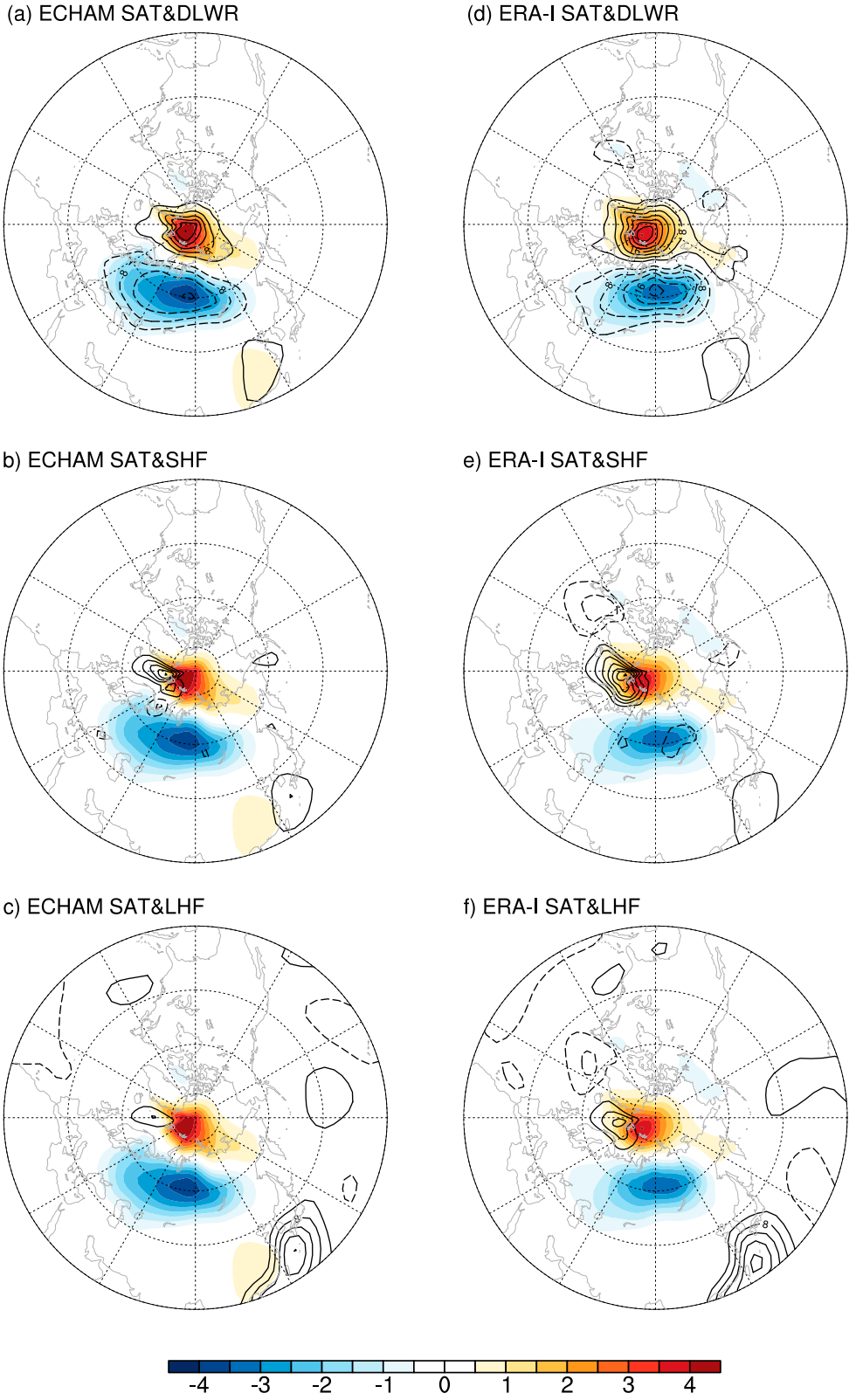

FIG. 15. Regressions of intraseasonal anomalous SAT (shading; K) along with (top) DLWR (W m^{-2}), (middle) surface sensible heat fluxes, (bottom) surface sensible heat fluxes, onto the normalized PC_1 of the leading intraseasonal SAT mode at day 0 in (a)–(c) ECHAM simulations and (d)–(f) ERA-I. All contours are plotted with intervals of 3 W m^{-2}.

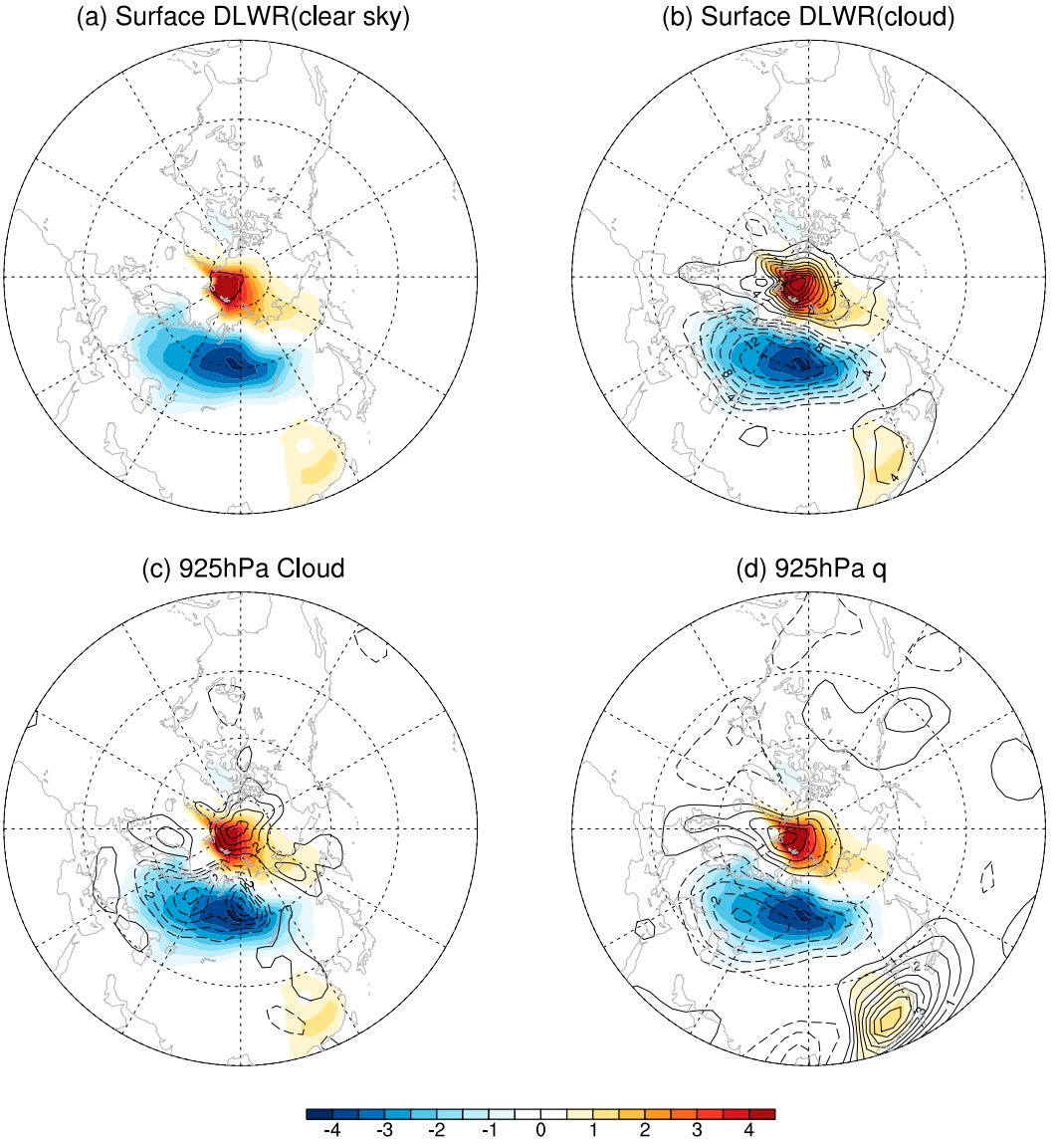

FIG. 16. Regressed intraseasonal anomalous SAT (shadings; K) at day 0 along with contours for (a) clear-sky and (b) cloudy-sky surface DLWR (W m^{-2}), (c) cloud fraction at 925 hPa (%), and (d) specific humidity (0.1 g kg^{-1}) associated with the leading intraseasonal SAT mode based on ECHAM GCM simulations.

largely similar to those in the control run (Fig. 17a) and observations (Fig. 3a). The vertical structure of T and circulation anomalies associated with the leading SAT mode in the "no_tropics" experiment are also very similar to those in the control experiment over the mid- to high latitudes (cf. Figs. 17d,f). These results are largely in agreement with previous studies that during winter the regions affected by the tropical convection are mainly confined to south of 30°N on both interannual and intraseasonal time scales (Zhang et al. 1996; Zhang et al. 2015; Zhang and Sumi 2002). Additionally, no significant impacts on T and circulation anomalies in the lower troposphere are found in the "no_strato" experiment despite the removal of the stratospheric influences above 100 hPa (Fig. 17e). Moreover, the southward WAFs from the Arctic to north Eurasia at 250 hPa which tend to be critical in sustaining the negative Z anomalies over Eurasia as discussed in both ERA-I (Fig. 6) and ECHAM control experiment (Fig. 11) are also largely captured in "no_strato" and "no_tropics" experiments (Figs. 17i,h, only patterns at day 0 shown). All these results suggest that influences from tropical convective activity and the stratosphere may not be essential in driving the leading intraseasonal SAT mode over Eurasia and the Arctic region.

5. Conclusions

Evolution characteristics, vertical structure, and key processes associated with the leading intraseasonal SAT variability

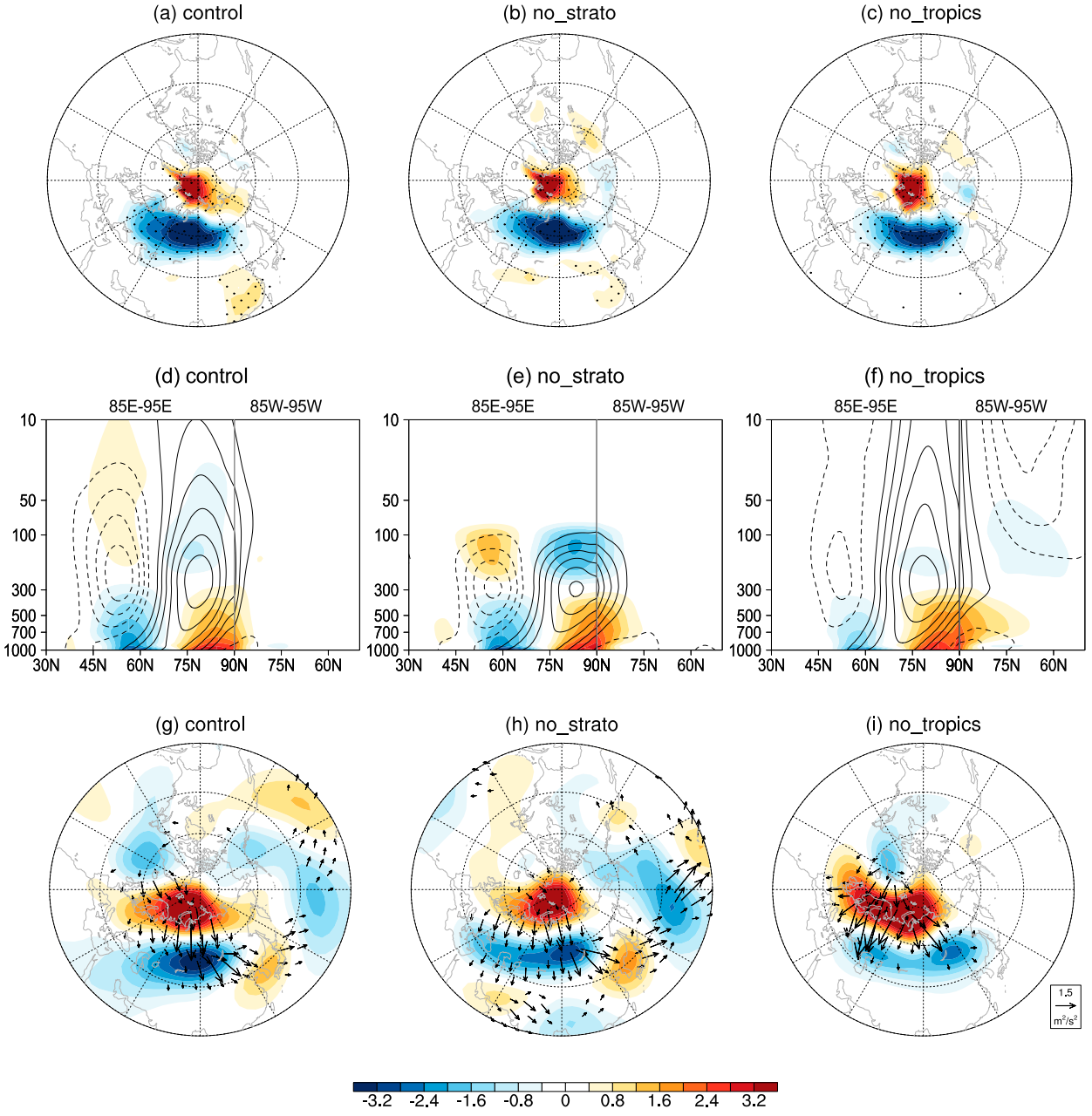

FIG. 17. Regressed intraseasonal anomalies associated with leading intraseasonal SAT mode at day 0: (a)–(c) SAT (shadings; K with intervals of 0.4 K), (d)–(f) height–latitude cross sections of T (shadings; K with intervals of 0.4 K) and Z (contours; gpm with intervals of 10 gpm), and (g)–(i) Z (gpm; shading) and horizontal wave activity flux ($m^2\ s^{-2}$; vectors) at 250 hPa, based on ECHAM simulations in the (left) control experiment, (middle) "no_strato" experiment, and (right) "no_tropics" experiment. The black dots in (a)–(c) denote the areas that are statistically significant at the 95% confidence level.

mode over Eurasia and the Arctic region during boreal winter are examined in this study. The leading intraseasonal SAT mode is characterized by a dipole structure with opposite signs of SAT anomalies over the Arctic and north Eurasia. Positive SAT anomalies over the Arctic and cold anomalies over Eurasia associated with this leading SAT mode are linked with each other by an anomalous high centered near the BKS region. Surface temperature anomalies associated with the leading SAT mode are coupled with temperature anomalies in the troposphere extending from the surface to 300 hPa with decreasing amplitude with height, and temperature anomalies with an opposite sign above 300 hPa. A deep anomalous circulation pattern, stretching from surface all the way into the stratosphere

with the maximum geopotential height near 300 hPa, is found to be coupled with the leading intraseasonal SAT mode.

In addition to its significant influences on local SAT over the mid- to high latitudes over the Eurasian sector, this leading intraseasonal SAT mode also exhibits strong modulations on SAT anomalies in remote areas including the East Asia monsoon region, possibly through the southeastward migration of this intraseasonal SAT mode. Meanwhile, the leading intraseasonal SAT mode is also closely associated with sea ice variability over the BKS region. Reduced sea ice in the BKS region is observed in association with warm anomalies over the Arctic and cold anomalies over Eurasia of the intraseasonal SAT mode. As the maximum of reduced SIC over BKS slightly lags the circulation and SAT anomalies associated with the intraseasonal SAT mode, the sea ice variability can be a response to circulation but its feedback onto the circulation and thus SAT anomalies cannot be excluded.

The observed evolution and spatial distribution of the leading intraseasonal SAT mode and associated air temperature anomalies in the troposphere over the Arctic and Eurasia are largely well simulated in the ECHAM AGCM, although the observed linkage in T and circulation anomalies between Eurasia and NA continents associated the intraseasonal SAT mode is not captured in simulations. Meanwhile, possibly due to the low-top configuration of the ECHAM GCM used in this study, the observed downward extension of geopotential height anomalies from the stratosphere to lower troposphere during the onset the intraseasonal SAT anomalies is also not represented in model simulations. Since the ECHAM AGCM is forced by climatological monthly mean SST and sea ice, this result indicates that the intraseasonal variability in SST and Arctic sea ice is not essential in driving this leading intraseasonal SAT mode. Based on ECHAM simulations, the underlying physical mechanisms that maintain the leading SAT variability mode are further investigated. By diagnosing the thermodynamic budget based on the temperature equation, it is found that the dynamical processes play a critical role for temperature anomalies in the troposphere associated with the SAT mode, with horizontal advection as the primary contributing term. The northerly wind anomalies in the eastern flank of the anomalous high over north Eurasia are conducive to bringing cold air from the Arctic toward the mid- to high latitudes, while the southerly wind anomalies on the western flank of the anomalous high brings warmer air in the mid- to high latitudes toward the Arctic. Model simulations illustrate that both the convective and radiative effects are not critical in sustaining the intraseasonal temperature variability. On the other hand, the surface energy budget suggests that surface warming (cooling) associated with the leading intraseasonal SAT mode is mainly due to the enhanced (reduced) surface DLWR. Further analysis suggests that the variability of surface DLWR is mainly induced by variability in clouds, which is in turn closely linked to lower-tropospheric moisture anomalies due to the horizontal moisture advection. Over the regions corresponding to warm (cold) air temperature anomalies in the lower troposphere, a similar moisture advection process as for the T anomalies will generate enhanced (reduced) moisture anomalies along with increased (decreased) cloudiness (Fig. 16), which can further lead to enhanced (reduced) DLWR and thus surface warming (cooling). Instead, model simulations indicate that the vertical temperature mixing is not important in coupling temperature anomalies in the lower troposphere and surface temperature as previously hypothesized on the longer time scales (e.g., Vargas Zeppetello et al. 2019).

To verify whether tropical MJO convective activities or stratospheric processes are essential to trigger the intraseasonal SAT mode, two additional model experiments are conducted by excluding influences of tropical variability and the stratosphere using a nudging approach. Our results show that the effects of tropical and stratosphere processes are not essential for the leading intraseasonal SAT variability mode during boreal winter over Eurasia and the Arctic region. In other words, the leading intraseasonal SAT mode can be generated by internal atmospheric processes over the mid- to high latitudes in the troposphere, possibly associated with processes underlying the formation of the blocking systems over Eurasia as previously reported (e.g., Takaya and Nakamura 2005; Luo et al. 2016; Kim et al. 2021). Further investigations are warranted to understand how these synoptic Rossby wave events are modulated on a subseasonal time scale. Also note that despite the model results in this study, possible roles of tropical and stratospheric forcing, as well as Arctic sea ice variability, on the intraseasonal SAT variability over Eurasia and the Arctic region cannot be excluded in the observations.

Acknowledgments. We greatly appreciate insightful comments from three anonymous reviewers that led to significant improvement of an earlier version of this manuscript. This study is jointly supported by the National Natural Science Foundation of China (41790472) and the National Key R&D Program of China (2016YFA0600602). XJ acknowledges support by the NOAA Climate Program Office under Awards NA17OAR4310261. GC is supported by NSF Grant AGS-1832842. The authors want to acknowledge Dr. Qinghua Ding for his help with the nudging approach when conducting ECHAM model experiments. The ERA-Interim reanalysis data can be obtained from the following website: http://apps.ecmwf.int/datasets/.

REFERENCES

Abdillah, M. R., Y. Kanno, and T. Iwasaki, 2018: Tropical–extratropical interactions associated with East Asian cold air outbreaks. Part II: Intraseasonal variation. *J. Climate*, **31**, 473–490, https://doi.org/10.1175/JCLI-D-17-0147.1.

Baxter, S., S. Weaver, J. Gottschalck, and Y. Xue, 2014: Pentad evolution of wintertime impacts of the Madden–Julian oscillation over the contiguous United States. *J. Climate*, **27**, 7356–7367, https://doi.org/10.1175/JCLI-D-14-00105.1.

Blackport, R., and J. A. Screen, 2020: Insignificant effect of Arctic amplification on the amplitude of midlatitude atmospheric waves. *Sci. Adv.*, **6**, eaay2880, https://doi.org/10.1126/sciadv.aay2880.

——, ——, K. van der Wiel, and R. Bintanja, 2019: Minimal influence of reduced Arctic sea ice on coincident cold winters in mid-latitudes. *Nat. Climate Change*, **9**, 697–704, https://doi.org/10.1038/s41558-019-0551-4.

Cassou, C., 2008: Intraseasonal interaction between the Madden–Julian oscillation and the North Atlantic Oscillation. *Nature*, **455**, 523–527, https://doi.org/10.1038/nature07286.

Clark, J. P., and S. B. Feldstein, 2019: What drives the North Atlantic Oscillation's temperature anomaly pattern? Part I: The growth and decay of the surface air temperature anomalies. *J. Atmos. Sci.*, **77**, 185–198, https://doi.org/10.1175/JAS-D-19-0027.1.

Cui, J., S. Yang, and T. Li, 2020: The influence of the Madden–Julian oscillation on high-latitude surface air temperature during boreal winter. *Dyn. Atmos. Oceans*, **90**, 101141, https://doi.org/10.1016/j.dynatmoce.2020.101141.

Dee, D. P., and Coauthors, 2011: The ERA-Interim reanalysis: Configuration and performance of the data assimilation system. *Quart. J. Roy. Meteor. Soc.*, **137**, 553–597, https://doi.org/10.1002/qj.828.

Deng, J., A. Dai, and D. Chyi, 2020: Northern Hemisphere winter air temperature patterns and their associated atmospheric and ocean conditions. *J. Climate*, **33**, 6165–6186, https://doi.org/10.1175/JCLI-D-19-0533.1.

Ding, Q., and Coauthors, 2017: Influence of high-latitude atmospheric circulation changes on summertime Arctic sea ice. *Nat. Climate Change*, **7**, 289–295, https://doi.org/10.1038/nclimate3241.

Duchon, C. E., 1979: Lanczos filtering in one and two dimensions. *J. Appl. Meteor. Climatol.*, **18**, 1016–1022, https://doi.org/10.1175/1520-0450(1979)018<1016:LFIOAT>2.0.CO;2.

Geng, X., W. Zhang, M. F. Stuecker, and F.-F. Jin, 2017: Strong sub-seasonal wintertime cooling over East Asia and Northern Europe associated with super El Niño events. *Sci. Rep.*, **7**, 3770, https://doi.org/10.1038/s41598-017-03977-2.

Gong, D.-Y., S.-W. Wang, and J.-H. Zhu, 2001: East Asian winter monsoon and Arctic Oscillation. *Geophys. Res. Lett.*, **28**, 2073–2076, https://doi.org/10.1029/2000GL012311.

Green, M. R., and J. C. Furtado, 2019: Evaluating the joint influence of the Madden–Julian oscillation and the stratospheric polar vortex on weather patterns in the Northern Hemisphere. *J. Geophys. Res. Atmos.*, **124**, 11 693–11 709, https://doi.org/10.1029/2019JD030771.

Guan, W., X. Jiang, X. Ren, G. Chen, and Q. Ding, 2020a: Role of atmospheric variability in driving the "warm-Arctic, cold-continent" pattern over the North America sector and sea ice variability over the Chukchi–Bering Sea. *Geophys. Res. Lett.*, **47**, e2020GL088599, https://doi.org/10.1029/2020GL088599.

——, ——, ——, ——, P. Lin, and H. Lin, 2020b: The leading intraseasonal variability mode of wintertime surface air temperature over the North American sector. *J. Climate*, **33**, 9287–9306, https://doi.org/10.1175/JCLI-D-20-0096.1.

He, J., H. Lin, and Z. Wu, 2011: Another look at influences of the Madden–Julian oscillation on the wintertime East Asian weather. *J. Geophys. Res.*, **116**, D03109, https://doi.org/10.1029/2010JD014787.

Honda, M., J. Inoue, and S. Yamane, 2009: Influence of low Arctic sea-ice minima on anomalously cold Eurasian winters. *Geophys. Res. Lett.*, **36**, L08707, https://doi.org/10.1029/2008GL037079.

Huang, J., and W. Tian, 2019: Eurasian cold air outbreaks under different Arctic stratospheric polar vortex strengths. *J. Atmos. Sci.*, **76**, 1245–1264, https://doi.org/10.1175/JAS-D-18-0285.1.

Inoue, J., M. E. Hori, and K. Takaya, 2012: The role of Barents sea ice in the wintertime cyclone track and emergence of a warm-Arctic cold-Siberian anomaly. *J. Climate*, **25**, 2561–2568, https://doi.org/10.1175/JCLI-D-11-00449.1.

Jeong, J.-H., C.-H. Ho, B.-M. Kim, and W.-T. Kwon, 2005: Influence of the Madden–Julian oscillation on wintertime surface air temperature and cold surges in East Asia. *J. Geophys. Res.*, **110**, D11104, https://doi.org/10.1029/2004JD005408.

Jiang, X., E. Maloney, and H. Su, 2020: Large-scale controls of propagation of the Madden–Julian Oscillation. *npj Climate Atmos. Sci.*, **3**, 29, https://doi.org/10.1038/s41612-020-00134-x.

Jiang, Z., S. B. Feldstein, and S. Lee, 2017: The relationship between the Madden–Julian oscillation and the North Atlantic Oscillation. *Quart. J. Roy. Meteor. Soc.*, **143**, 240–250, https://doi.org/10.1002/qj.2917.

Kim, B.-M., S.-W. Son, S.-K. Min, J.-H. Jeong, S.-J. Kim, X. Zhang, T. Shim, and J.-H. Yoon, 2014: Weakening of the stratospheric polar vortex by Arctic sea-ice loss. *Nat. Commun.*, **5**, 4646, https://doi.org/10.1038/ncomms5646.

Kim, H.-J., S.-W. Son, W. Moon, J.-S. Kug, and J. Hwang, 2021: Subseasonal relationship between Arctic and Eurasian surface air temperature. *Sci. Rep.*, **11**, 4081, https://doi.org/10.1038/s41598-021-83486-5.

Kolstad, E. W., T. Breiteig, and A. A. Scaife, 2010: The association between stratospheric weak polar vortex events and cold air outbreaks in the Northern Hemisphere. *Quart. J. Roy. Meteor. Soc.*, **136**, 886–893, https://doi.org/10.1002/qj.620.

Kretschmer, M., D. Coumou, L. Agel, M. Barlow, E. Tziperman, and J. Cohen, 2018: More-persistent weak stratospheric polar vortex states linked to cold extremes. *Bull. Amer. Meteor. Soc.*, **99**, 49–60, https://doi.org/10.1175/BAMS-D-16-0259.1.

Lang, A. L., K. Pegion, and E. A. Barnes, 2020: Introduction to special collection: "Bridging Weather and Climate: Subseasonal-to-Seasonal (S2S) Prediction." *J. Geophys. Res. Atmos.*, **125**, e2019JD031833, https://doi.org/10.1029/2019JD031833.

Lee, S., T. Gong, N. Johnson, S. B. Feldstein, and D. Pollard, 2011: On the possible link between tropical convection and the Northern Hemisphere Arctic surface air temperature change between 1958 and 2001. *J. Climate*, **24**, 4350–4367, https://doi.org/10.1175/2011JCLI4003.1.

L'Heureux, M. L., and R. W. Higgins, 2008: Boreal winter links between the Madden–Julian oscillation and the Arctic Oscillation. *J. Climate*, **21**, 3040–3050, https://doi.org/10.1175/2007JCLI1955.1.

Li, T., J. Ling, and P.-C. Hsu, 2020: Madden–Julian oscillation: Its discovery, dynamics, and impact on East Asia. *J. Meteor. Res.*, **34**, 20–42, https://doi.org/10.1007/s13351-020-9153-3.

Lin, H., 2015: Subseasonal variability of North American wintertime surface air temperature. *Climate Dyn.*, **45**, 1137–1155, https://doi.org/10.1007/s00382-014-2363-6.

——, 2018: Predicting the dominant patterns of subseasonal variability of wintertime surface air temperature in extratropical Northern Hemisphere. *Geophys. Res. Lett.*, **45**, 4381–4389, https://doi.org/10.1029/2018GL077509.

——, and G. Brunet, 2009: The influence of the Madden–Julian oscillation on Canadian wintertime surface air temperature. *Mon. Wea. Rev.*, **137**, 2250–2262, https://doi.org/10.1175/2009MWR2831.1.

——, ——, and J. Derome, 2009: An observed connection between the North Atlantic Oscillation and the Madden–

Julian oscillation. *J. Climate*, **22**, 364–380, https://doi.org/10.1175/2008JCLI2515.1.

Luo, D., Y. Xiao, Y. Yao, A. Dai, I. Simmonds, and C. L. E. Franzke, 2016: Impact of Ural blocking on winter warm Arctic–cold Eurasian anomalies. Part I: Blocking-induced amplification. *J. Climate*, **29**, 3925–3947, https://doi.org/10.1175/JCLI-D-15-0611.1.

Madden, R. A., and P. R. Julian, 1971: Detection of a 40–50 day oscillation in the zonal wind in the tropical Pacific. *J. Atmos. Sci.*, **28**, 702–708, https://doi.org/10.1175/1520-0469(1971)028<0702:DOADOI>2.0.CO;2.

——, and ——, 1972: Description of global-scale circulation cells in the tropics with a 40–50 day period. *J. Atmos. Sci.*, **29**, 1109–1123, https://doi.org/10.1175/1520-0469(1972)029<1109:DOGSCC>2.0.CO;2.

Mori, M., M. Watanabe, H. Shiogama, J. Inoue, and M. Kimoto, 2014: Robust Arctic sea-ice influence on the frequent Eurasian cold winters in past decades. *Nat. Geosci.*, **7**, 869–873, https://doi.org/10.1038/ngeo2277.

——, Y. Kosaka, M. Watanabe, H. Nakamura, and M. Kimoto, 2019: A reconciled estimate of the influence of Arctic sea-ice loss on recent Eurasian cooling. *Nat. Climate Change*, **9**, 123–129, https://doi.org/10.1038/s41558-018-0379-3.

Nakamura, T., K. Yamazaki, K. Iwamoto, M. Honda, Y. Miyoshi, Y. Ogawa, and J. Ukita, 2015: A negative phase shift of the winter AO/NAO due to the recent Arctic sea-ice reduction in late autumn. *J. Geophys. Res. Atmos.*, **120**, 3209–3227, https://doi.org/10.1002/2014JD022848.

——, ——, ——, ——, ——, ——, Y. Tomikawa, and J. Ukita, 2016: The stratospheric pathway for Arctic impacts on midlatitude climate. *Geophys. Res. Lett.*, **43**, 3494–3501, https://doi.org/10.1002/2016GL068330.

National Academies of Sciences, Engineering and Medicine, 2016: *Next Generation Earth System Prediction: Strategies for Subseasonal to Seasonal Forecasts*. The National Academies Press, 350 pp.

Nordeng, T. E., 1994: Extended versions of the convective parametrization scheme at ECMWF and their impact on the mean and transient activity of the model in the tropics. ECMWF Tech. Memo. 206, 41 pp., https://www.ecmwf.int/node/11393.

Park, T.-W., C.-H. Ho, S. Yang, and J.-H. Jeong, 2010: Influences of Arctic Oscillation and Madden–Julian oscillation on cold surges and heavy snowfalls over Korea: A case study for the winter of 2009–2010. *J. Geophys. Res.*, **115**, D23122, https://doi.org/10.1029/2010JD014794.

——, ——, and ——, 2011: Relationship between the Arctic Oscillation and cold surges over East Asia. *J. Climate*, **24**, 68–83, https://doi.org/10.1175/2010JCLI3529.1.

Peng, C., K. Fan, and H. Dai, 2019: Sub seasonal variations of weak stratospheric polar vortex in December and its impact on Eurasian air temperature. *Atmos. Oceanic Sci. Lett.*, **12**, 369–375, https://doi.org/10.1080/16742834.2019.1640053.

Riddle, E. E., M. B. Stoner, N. C. Johnson, M. L. L'Heureux, D. C. Collins, and S. B. Feldstein, 2013: The impact of the MJO on clusters of wintertime circulation anomalies over the North American region. *Climate Dyn.*, **40**, 1749–1766, https://doi.org/10.1007/s00382-012-1493-y.

Roeckner, E., and Coauthors, 1996: The atmospheric general circulation model ECHAM-4: Model description and simulation of present-day climate. Max-Planck-Institute for Meteorology Rep. 218, 94 pp., http://www.mpimet.mpg.de/fileadmin/publikationen/Reports/MPI-Report_218.pdf

Seo, K.-H., H.-J. Lee, and D. M. W. Frierson, 2016: Unraveling the teleconnection mechanisms that induce wintertime temperature anomalies over the Northern Hemisphere continents in response to the MJO. *J. Atmos. Sci.*, **73**, 3557–3571, https://doi.org/10.1175/JAS-D-16-0036.1.

Song, L., and R. Wu, 2018: Comparison of intraseasonal East Asian winter cold temperature anomalies in positive and negative phases of the Arctic Oscillation. *J. Geophys. Res. Atmos.*, **123**, 8518–8537, https://doi.org/10.1029/2018JD028343.

——, and ——, 2019a: Precursory signals of East Asian winter cold anomalies in stratospheric planetary wave pattern. *Climate Dyn.*, **52**, 5965–5983, https://doi.org/10.1007/s00382-018-4491-x.

——, and ——, 2019b: Impacts of MJO convection over the maritime continent on Eastern China cold temperatures. *J. Climate*, **32**, 3429–3449, https://doi.org/10.1175/JCLI-D-18-0545.1.

——, and ——, 2019c: Combined effects of the MJO and the Arctic Oscillation on the intraseasonal Eastern China winter temperature variations. *J. Climate*, **32**, 2295–2311, https://doi.org/10.1175/JCLI-D-18-0625.1.

——, and ——, 2020: Distinct Eurasian climate anomalies associated with strong and weak MJO events. *Int. J. Climatol.*, **40**, 6666–6674, https://doi.org/10.1002/joc.6630.

Sorokina, S. A., C. Li, J. J. Wettstein, and N. G. Kvamstø, 2016: Observed atmospheric coupling between Barents Sea ice and the warm-Arctic cold-Siberian anomaly pattern. *J. Climate*, **29**, 495–511, https://doi.org/10.1175/JCLI-D-15-0046.1.

Sun, L., C. Deser, and R. A. Tomas, 2015: Mechanisms of stratospheric and tropospheric circulation response to projected Arctic sea ice loss. *J. Climate*, **28**, 7824–7845, https://doi.org/10.1175/JCLI-D-15-0169.1.

Sung, M.-K., S.-W. Son, C. Yoo, J. Hwang, and S.-I. An, 2021: Seesawing of winter temperature extremes between East Asia and North America. *J. Climate*, **34**, 4423–4434, https://doi.org/10.1175/JCLI-D-20-0789.1.

Takaya, K., and H. Nakamura, 2001: A formulation of a phase-independent wave-activity flux for stationary and migratory quasigeostrophic eddies on a zonally varying basic flow. *J. Atmos. Sci.*, **58**, 608–627, https://doi.org/10.1175/1520-0469(2001)058<0608:AFOAPI>2.0.CO;2.

——, and ——, 2005: Mechanisms of intraseasonal amplification of the cold Siberian high. *J. Atmos. Sci.*, **62**, 4423–4440, https://doi.org/10.1175/JAS3629.1.

Tiedtke, M., 1989: A comprehensive mass flux scheme for cumulus parameterization in large-scale models. *Mon. Wea. Rev.*, **117**, 1779–1800, https://doi.org/10.1175/1520-0493(1989)117<1779:ACMFSF>2.0.CO;2.

Vargas Zeppetello, L. R., A. Donohoe, and D. S. Battisti, 2019: Does surface temperature respond to or determine downwelling longwave radiation? *Geophys. Res. Lett.*, **46**, 2781–2789, https://doi.org/10.1029/2019GL082220.

Vecchi, G. A., and N. A. Bond, 2004: The Madden–Julian oscillation (MJO) and northern high latitude wintertime surface air temperatures. *Geophys. Res. Lett.*, **31**, L04104, https://doi.org/10.1029/2003GL018645.

Vitart, F., and A. W. Robertson, 2018: The sub-seasonal to seasonal prediction project (S2S) and the prediction of extreme events. *npj Climate Atmos. Sci.*, **1**, 3, https://doi.org/10.1038/s41612-018-0013-0.

——, and Coauthors, 2017: The Subseasonal to Seasonal (S2S) prediction project database. *Bull. Amer. Meteor. Soc.*, **98**, 163–173, https://doi.org/10.1175/BAMS-D-16-0017.1.

Wheeler, M. C., and H. H. Hendon, 2004: An all-season real-time multivariate MJO index: Development of an index for monitoring and prediction. *Mon. Wea. Rev.*, **132**, 1917–1932, https://doi.org/10.1175/1520-0493(2004)132<1917:AARMMI>2.0.CO;2.

Woo, S.-H., B.-M. Kim, and J.-S. Kug, 2015: Temperature variation over East Asia during the life cycle of weak stratospheric polar vortex. *J. Climate*, **28**, 5857–5872, https://doi.org/10.1175/JCLI-D-14-00790.1.

Xiang, B., S.-J. Lin, M. Zhao, N. C. Johnson, X. Yang, and X. Jiang, 2019: Subseasonal week 3–5 surface air temperature prediction during boreal wintertime in a GFDL model. *Geophys. Res. Lett.*, **46**, 416–425, https://doi.org/10.1029/2018GL081314.

——, Y. Q. Sun, J.-H. Chen, N. C. Johnson, and X. Jiang, 2020: Subseasonal prediction of land cold extremes in boreal wintertime. *J. Geophys. Res. Atmos.*, **125**, e2020JD032670, https://doi.org/10.1029/2020JD032670.

Yang, S., and T. Li, 2016: Intraseasonal variability of air temperature over the mid-high latitude Eurasia in boreal winter. *Climate Dyn.*, **47**, 2155–2175, https://doi.org/10.1007/s00382-015-2956-8.

——, Z. Zhu, J. Cui, and Y. Yang, 2019: Regulation of the intraseasonal oscillation over mid-to-high latitude Eurasia on winter surface air temperature over China. *Dyn. Atmos. Oceans*, **86**, 63–72, https://doi.org/10.1016/j.dynatmoce.2019.03.003.

Yao, S., Q. Sun, Q. Huang, and P. Chu, 2016: The 10–30-day intraseasonal variation of the East Asian winter monsoon: The temperature mode. *Dyn. Atmos. Oceans*, **75**, 91–101, https://doi.org/10.1016/j.dynatmoce.2016.07.001.

——, Q. Tong, T. Li, and K. Gong, 2020: The 10–30-day oscillation of winter rainfall in southern China and its relationship with circulation patterns in different latitudes. *Int. J. Climatol.*, **40**, 3268–3280, https://doi.org/10.1002/joc.6396.

Yao, Y., H. Lin, and Q. Wu, 2015: Subseasonal variability of precipitation in China during boreal winter. *J. Climate*, **28**, 6548–6559, https://doi.org/10.1175/JCLI-D-15-0033.1.

Ye, K., and T. Jung, 2019: How strong is influence of the tropics and midlatitudes on the Arctic atmospheric circulation and climate change? *Geophys. Res. Lett.*, **46**, 4942–4952, https://doi.org/10.1029/2019GL082391.

Yoo, C., S. Lee, and S. B. Feldstein, 2012: Mechanisms of Arctic surface air temperature change in response to the Madden–Julian oscillation. *J. Climate*, **25**, 5777–5790, https://doi.org/10.1175/JCLI-D-11-00566.1.

Zhang, P., Y. Wu, I. R. Simpson, K. L. Smith, X. Zhang, B. De, and P. Callaghan, 2018: A stratospheric pathway linking a colder Siberia to Barents-Kara Sea sea ice loss. *Sci. Adv.*, **4**, eaat6025, https://doi.org/10.1126/sciadv.aat6025.

Zhang, R., and A. Sumi, 2002: Moisture circulation over East Asia during El Niño episode in northern winter, spring and autumn. *J. Meteor. Soc. Japan*, **80**, 213–227, https://doi.org/10.2151/jmsj.80.213.

——, ——, and M. Kimoto, 1996: Impact of El Niño on the East Asian monsoon: A diagnostic study of the '86/87 and '91/92 events. *J. Meteor. Soc. Japan*, **74**, 49–62, https://doi.org/10.2151/jmsj1965.74.1_49.

——, T. Li, M. Wen, and L. Liu, 2015: Role of intraseasonal oscillation in asymmetric impacts of El Niño and La Niña on the rainfall over southern China in boreal winter. *Climate Dyn.*, **45**, 559–567, https://doi.org/10.1007/s00382-014-2207-4.

Zheng, C., E. Kar-Man Chang, H.-M. Kim, M. Zhang, and W. Wang, 2018: Impacts of the Madden–Julian oscillation on storm-track activity, surface air temperature, and precipitation over North America. *J. Climate*, **31**, 6113–6134, https://doi.org/10.1175/JCLI-D-17-0534.1.

Zhou, S., M. L'Heureux, S. Weaver, and A. Kumar, 2012: A composite study of the MJO influence on the surface air temperature and precipitation over the Continental United States. *Climate Dyn.*, **38**, 1459–1471, https://doi.org/10.1007/s00382-011-1001-9.